https://doi.org/10.1016/j.engstruct.2021.112493

Probabilistic performance of Coastal Bridges under Hurricane Waves using Experimental and 3D Numerical Investigations

Deming Zhu[1], Peng Yuan[2], and You Dong[3, *]

Abstract

This paper proposes a comprehensive framework for performance and reliability analyses of coastal bridges under hurricane surge and waves, including a three-dimensional (3D) Computational Fluid Dynamics (CFD) model to simulate the wave-structure interaction, laboratory experiments to improve the model accuracy, a 3D Finite Element Model (FEM) to evaluate bridge and component responses, surrogate models for performance prediction, as well as effects of uncertainties and climate changes in long-term vulnerability analyses. The experimental validation ensures the credibility of the established model and computational results. For accurate and efficient quantification of the structural responses under different surge and wave conditions, surrogate models with different parameters are introduced for investigated scenarios, which could not be well predicted by using existing methods. Based on the detailed 3D CFD and FEM results, a new component-level overturning failure mode of a bridge subjected to the hurricane is developed by considering wave force, overturning moment, bearing damages, and uncertainties in structural and hazard parameters. Given fragility surface and potential changing climate scenario, long-term reliability analysis is performed. The established framework could be accurately and widely applied to other bridges and hurricane scenarios by adjusting the model and experimental parameters. This study could help in exploring the resistance of coastal bridges against natural hazards, and in developing specifications to mitigate future hurricane risk.

Keywords: Coastal bridges; 3D numerical models; Laboratory experiment; Overturning effects; Bearing performance; Probabilistic fragility model.

---

[1] Ph.D. student, The Hong Kong Polytechnic University, Department of Civil and Environmental Engineering, Hung Hom, Kowloon, Hong Kong, deming.zhu@connect.polyu.hk.

[2] Postdoctoral Fellow, The Hong Kong Polytechnic University, Department of Civil and Environmental Engineering, Hung Hom, Kowloon, Hong Kong, peng10.yuan@polyu.edu.hk.

[3] Assistant Professor of Structural Engineering, The Hong Kong Polytechnic University, Department of Civil and Environmental Engineering, Hung Hom, Kowloon, Hong Kong, you.dong@polyu.edu.hk.

*Corresponding Author.

1. Introduction

Due to the climate change scenario in recent years, hurricanes have a devastating impact on coastal communities, threatening public life and property. For instance, Hurricane Wilma in 2005 attacked the US and caused 23 deaths and a total loss of $28.1 billion (2005 USD) [1]. Typhoon Hato in 2017 struck Macau and led to 10 fatalities and a $1.42 billion loss (2017 USD) [2]. The infrastructures, especially for those coastal bridges, are particularly susceptible to damage for their inadequate design. Under hurricane events, damaged bridges may not only result in traffic disruption and economic loss, but also the subsequent rescue and material transportation problem. Reliability assessment of the coastal bridge under hurricanes is of vital importance for enhancing resistance and resilience capacity of coastal communities against natural hazards, and for developing structure specifications to mitigate future risks as well.

For systematic reliability analysis, the structural capacity and demand associated with failure mode should be identified, which require a deep exploration of the structural performance under hazards [3], [4]. Generally, a primary failure mode for coastal bridges under hurricane events is the deck unseating by comparing the uplift wave force with the deck weight [5]. For instance, [6] conducted laboratory experiments to measure the hurricane wave forces on the superstructure of coastal bridges. [7] tested the quasi-static wave forces on the bridge deck. However, an important thing that has often been neglected is the characteristic that the wave tends to impact the deck from only one side, causing an extreme force concentrated on the seaward side of the deck. Considering the large width of the deck, the uneven load distribution could lead to significant structural stability problems such as extreme overturning moment and component damage (*e.g.*, bearing). [8] tried to calculate the overturning moment from the measured wave loads but neglected the contribution of the horizontal force. [9] used a CFD model to compute the overturning moment, while the constraints of the bearings were not examined. Studies on the wave force distribution and overturning moment were very limited. Therefore, this study focuses on detailed structural performances under hurricane waves, including wave force, overturning moment, bearing damage, and failure sequence.

To explicitly assess the bridges and components performance under the relevant forces, the complex wave-structure interaction, such as the trapped air between the girders and the deck, should be well addressed. Traditional two-dimensional (2D) computational fluid dynamics (CFD) model has often been adopted to simulate the wave-structure interaction considering the high expense of prototype scale experiments [10]–[13]. Although several empirical formulas have been reached based on this method, the 2D model is limited in the longitudinal (z) axis in providing accurate results. [14] simulated the wave-bridge interaction and found there existed differences between their 2D computational results with the analytical ones. [9] conducted numerical research of solitary wave forces on bridges and pointed out the 2D numerical model may not fully capture the wave features. [15] concluded that simplification by using a 2D model could lead to errors, and a three-dimensional (3D) model should be studied for better simulation of the wave process. [16] examined 2D and 3D models with experimental measurements and proved the 3D model's better performance in simulating the trapped air and calculating wave load. Thus, a 3D CFD model is established in this study to investigate the wave-structure interaction and to measure the external wave loads on the bridge model. In addition, laboratory experiments are conducted in this study to improve and validate the numerical model considering the complicated hydrodynamic problem. The wave-induced forces are extracted from the CFD model and then imported into a 3D structural finite element model (FEM) for the investigated bridge. The established 3D FEM bridge model could compute structural responses and bearing performance of the bridge under wave impacts, comprehensively considering the effects of structural dimensions, bearing constraints, and material properties (e.g., stiffness, density, and elastic modulus).

On the other hand, a systematic probabilistic assessment framework of coastal bridges under hurricane waves has not been well established. Existing ones are established based on some general empirical formulas, neglecting the complex wave-structure interaction process and the component performance. For instance, [17] investigated damaged bridges during Hurricane Katrina, and qualitatively described bridge damage levels. [5] proposed the bridge deck unseating failure mode by comparing empirical wave forces and the static weight of the bridge. Furthermore, most previous studies focused on the deterministic performance assessment of the coastal bridge under wave loads, which does not allow uncertainty quantification associated with capacity and demand [18]–[21]. Only a few studies assessed the reliability of bridges under hurricanes [22]. [23] attempted to assess the vulnerability of the coastal bridge under hurricane events using multiple environmental parameters. [24] utilized surrogate models to evaluate the structural responses with different intensity measures based on a 2D model. [25] discussed uncertainties in demand and capacity models and pointed out that more studies should be conducted on the failure model at a structural component level. There also exist some other studies [26]–[30] on the reliability assessment of coastal bridges under hurricane wave loads. However, in these probabilistic studies, the overturning failure mechanism and performance of the components (*e.g.*, bearings) were not considered. To the best knowledge of the authors, there has been no study focusing on a systematic and detailed probabilistic performance assessment of coastal bridges under hurricane surge and waves using both experimental and numerical methods. Therefore, based on the 3D numerical and experimental investigations, this study develops a new component-level overturning failure mode of a bridge subjected to hurricane waves by considering the overturning moment, bearing damage, and uncertainties in structural capacity and demand.

Nowadays, climate change has an increasing impact on the built environment and civil infrastructure performance [31], [32]. There has been growing evidence that global climate change may affect both the frequency and severity of the extreme event from natural hazards [33], [34]. [35] estimated that hurricane speed may increase by 20% around the world in the 21st century. Australian Greenhouse office reported that the peak wind speed would increase by 2-5% by year 2030 and 5-10% by 2070. The IPCC (Intergovernmental Panel on Climate Change) also indicated that hurricane intensity and frequency may be affected by the increase of sea surface temperature. Under the climate change scenario, the increased vulnerability of civil infrastructure poses a significant challenge to city planners and bridge managers. Thus, studies are needed to assess the potential impact of climate change on the bridge vulnerability and reliability under hurricanes.

Overall, this paper proposes a comprehensive framework for performance, vulnerability, and reliability assessment of coastal bridges under hurricane surge and waves, and develops a novel component-level overturning failure mode. The framework, as shown in Fig. (1), includes an experimental verified 3D CFD model to investigate the fluid-structure interaction, a 3D FEM to evaluate bridge and component responses, surrogate models to predict structural performance, a probabilistic bridge fragility model considering the uncertainties associated with structural capacity and demand, as well as a long-term failure probability analysis considering climate change effect. The 3D CFD model and experimental measurement are introduced in section 2. The FEM setups and results are presented in section 3. The new component-level overturning failure mode and relative limit states are discussed in section 4. The probabilistic long-term failure probability is presented in section 5. Conclusions are drawn in section 6. The proposed framework can be used in reliability assessment of other structure and hazard types and extended to evaluate the effectiveness of alternative retrofit measures.

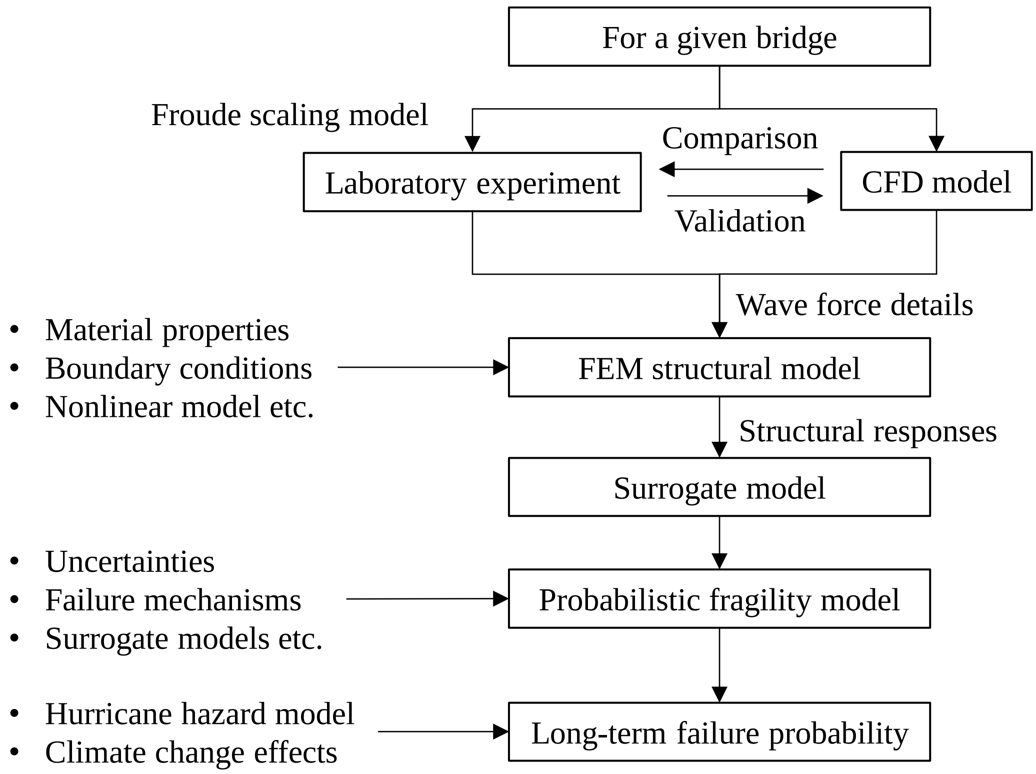

Fig. 1 Computational flowchart of the developed framework

2. 3D CFD modeling and experimental investigation on wave-structure interaction

In this section, the wave-structure interaction is studied with *ANSYS* Fluent. The traditional 2D CFD model could simulate the solitary wave but may yield errors due to the simplification in the longitudinal direction (z axis). A 2D model could not reflect the uneven wave force distribution on the deck, which is detrimental to the subsequent structural response analyses such as the bearing performance. The 3D model could better address the trapped air between the deck and girders, calculate wave load distribution, and thus provide more accurate results. Therefore, a 3D CFD model is established to investigate the hurricane wave for more accurate results.

Furthermore, laboratory experiments are adopted as an improvement and validation for the numerical model. The complex hydrodynamic problem, especially for the wave-structure interaction with trapped air in this study, could significantly influence the accuracy of the numerical model. Although there exist several theoretical models to describe the fluid motion, it requires specific analyses for the given case considering practical engineering issues. Laboratory experiments could provide insights into the characteristics of wave-structure interaction, as well as the basis of numerical simulation. Hence, experiments are conducted herein to measure the relevant load on the bridge and to validate the CFD model. With the established model, differences between the results from 2D and 3D models are compared, horizontal and vertical wave forces are computed, properties of wave forces are discussed.

For the ease of the following discussion, the bridge model is introduced first. Based on the reconnaissance report after hurricanes, most of the severely damaged bridges during hurricanes were simply supported concrete bridges, of which the old design cannot meet the requirement of extreme hurricane waves and climate change effects [36]. For illustrative purposes, the bridge model investigated herein is a typical simply supported bridge widely built in coastal regions as Fig. 2 (a). Detailed information and damage reports of this type of bridge could be found in [36]. The deck is supported by 6 bearings at each side, labeled from L1-L6 and R1-R6 as Fig. 2 (b). The water depth is assumed as 6 m, and clearance, which is the distance from the bottom of bridge girders to still water level before storm surge arrives, is set as 4 m.

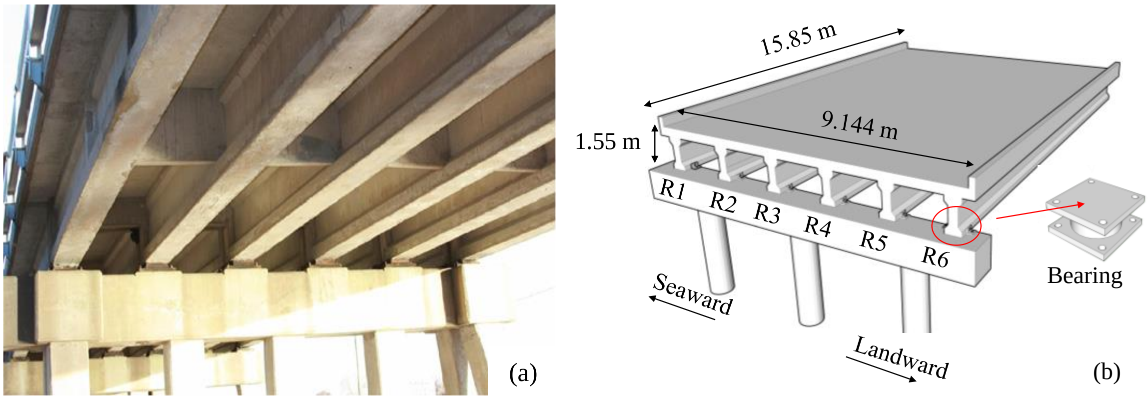

Fig. 2 (a) Simply supported bridge and (b) schematic diagram of the investigated bridge

2.1 3D CFD modeling and experimental validation

The boundary conditions of the CFD numerical domain in the *ANSYS* Fluent are shown in Fig. 3 (a). The numerical domain is 140 m in length (*x* direction), 20.85 m in width (*z* direction), and 30 m in height (*y* direction). The bridge is located 20 m from the inlet plane, and there is a 100-m long region between the bridge model and the outlet plane to minimize wave reflection effects. Note that only part of the numerical domain is shown in Fig. 3 for clear presentation. As indicated, plane ABCD is the velocity inlet; plane EFGH is the pressure outlet to keep the balanced pressures for the air and water zones; plane BCGF is set as pressure outlet with the constant atmosphere pressure (*i.e.*, 101,325 Pa); and others are set as no-slip stationary wall conditions. In the CFD model, the I-shaped girders are simplified to rectangular, which is a common method to reduce the high computational cost associated with hydrodynamics. The wave forces on the bridge deck are calculated as the sum of the dot product of the pressure and viscous forces on each face with the specified force vector [37]. The volume of fluid (VOF) method is used to determine the dynamic free surface, and two phases are included. Air is set as phase-1, the primary phase, and water-liquid is set as phase-2, the secondary phase. The shear-stress transport (SST k-ω) model is utilized as the turbulence closure for the Reynolds-averaged Navier-Stokes (RANS) equations.

In this study, the solitary wave theory is applied to simulate extreme waves, which is a widely accepted model to investigate hydrodynamic effects on coastal bridges in the engineering field [38]. In addition, a solitary wave has a relatively stable wave profile within processing [39], [40], which is beneficial to validate the CFD model using experiments and conduct the parametric study. The free surface profile η of the applied solitary wave theory is [41], [42]

$$\eta(x,t) = H \operatorname{sech}^2 \sqrt{\frac{3}{4}\frac{H}{D^3}}(x-ct) \tag{1}$$

$$t_0 = \frac{\tanh^{-1}(0.999)}{c\sqrt{\frac{3}{4}\frac{H}{D^3}}} = \frac{3.8}{c\sqrt{\frac{3}{4}\frac{H}{D^3}}} \tag{2}$$

where H = wave height; D = water depth; c = wave celerity; x = coordinate; and t_0 = the time interval between the wave crest and still water level. To meet the requirement of practical experimental and numerical tests, an approximate method of using three significant figures, *i.e.*, 0.999 in Eq. (2), is adopted to calculate the infinite solitary wave period [42]. The simplified wave period can be calculated as $2t_0$, and the wavelength λ equals the product of wave period and celerity.

In the numerical domain, a Boolean subtract is applied for the bridge model, and tetrahedron mesh is used to fit the irregular surface of the model. To ensure accuracy of the 3D numerical domain, a mesh sensitivity study is conducted, and different time steps are tested to satisfy the Courant Number [43]. After several calculations and comparisons for different mesh resolutions, the mesh size is determined as 0.6 m and the fixed time step is set as 0.01 s. The Courant Number is around 1/3. The generated mesh of the model is shown in Fig. 3 (b). Results of mesh sensitivity analysis are plotted in Fig. 3 (d). Little differences among each condition are observed. Before testing the wave-structure interaction, the authors examine the simulation stability of the generated solitary waves. After several calculations, the generated solitary waves could forward with a steady wave profile under a wave height to water depth ratio (H/D) from 0.2 – 0.6. Given further examinations, more H/D scenarios could be applicable in other studies. The measured water surface elevations in the numerical model are compared with analytical models. A typical case with D = 7.2 m and H = 4.8 m is shown in Fig. 3 (c), and good agreements are observed. The initial water depth is set as 6 m, and additional water depth (considering the effects of storm surge, tidal, and sea-level rise, *etc.*) ranges from 1 – 8 m, *i.e.*, the overall water depth D is from 7 – 14 m. Multiple wave heights are tested for each water depth with considering the H/D ratio.

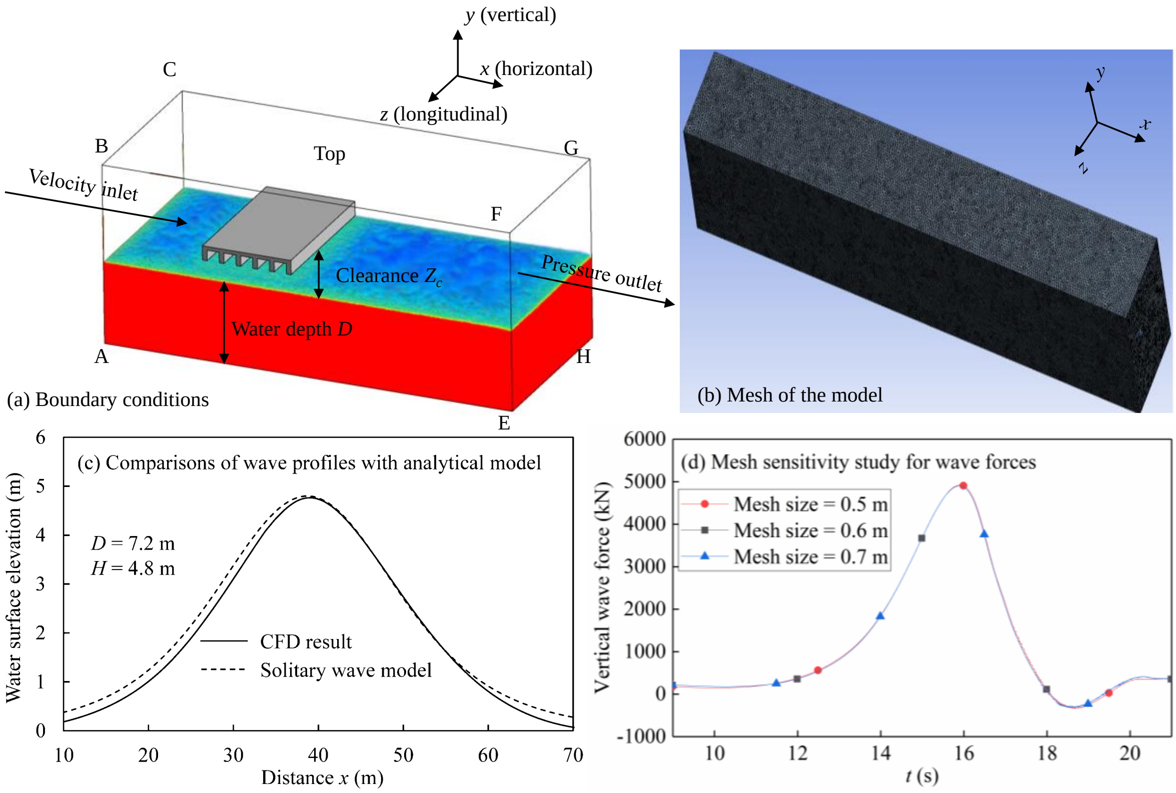

Fig. 3 (a) Boundary conditions of the 3D numerical domain; (b) generated mesh of the model; (c) comparisons of simulated wave profile with the analytical model; and (d) results of the mesh sensitivity analysis

A 1:30 scale experiment, which is designed according to the Froude scale model [44], is conducted in the wave channel at the Hydraulics Laboratory of the Hong Kong Polytechnic University. The wave channel is 30 m in length, 1.5 m in width, and 2 m in height as Fig. 4 (a). The Froude scale model [44] is suitable for phenomena where gravity and inertial forces are dominant, particularly for free surface flows (*e.g.*, coastal structures and waves). For a geometric scale ratio $\tau = L_m / L_p$ (model/prototype), other scale ratios can be derived from the Froude similarity, *e.g.*, velocity ratio = $\tau^{1/2}$, pressure ratio = τ, and force ratio = τ^3. The tested bridge model is made of acrylic board, 0.52 m in length and 0.32 m in width. A piston-type wavemaker is used to generate waves at one side of the wave channel using DHI's (Danish

Hydraulic Institute) control system. A wave attenuation slope is set at the end of the wave channel to minimize wave reflection effects. Water surface elevation is measured using capacitive wave height gauges. Three wave gauges are arranged as Fig. 4 (b). A multi-axis load cell is used to measure wave forces on the bridge model at a frequency of 100 Hz. The signal from the load cell sensor is converted to electrical signal ranging 0 ~ ± 5 V by a signal transmitter and then collected by a multi-channel data acquisition board. Instrument calibration is performed for all the wave gauges and load cell in *x*, *y*, and *z* directions, respectively. A schematic diagram of the wave channel and experimental setups is presented in Fig. 4 (c). After several tests, the piston type wave generator could generate stable solitary wave with a *H*/*D* ratio from 0.15 – 0.5.

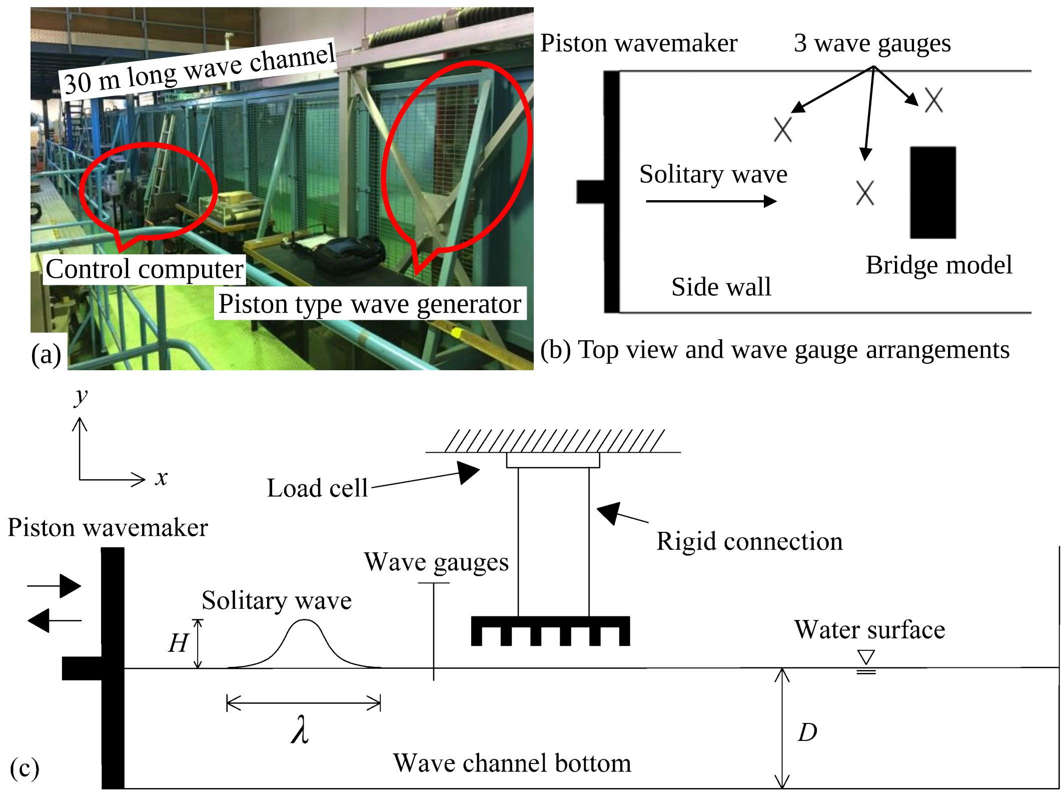

Fig. 4 (a) Photo of the 30 m long wave channel; (b) top view of the wave channel and arrangement of wave gauges; and (c) schematic diagram of experimental setups

Photos of two typical moments in the experiment test are shown in Fig. 5. The wave comes from the left side to the right side. When the water surface rises and reaches the deck, the water surface is broken by the bridge model, causing splashes as indicated in Fig. 5 (b). The solitary wave could not only exceed the top of the deck but also flow around the deck in the longitudinal direction (in z direction as indicated in Fig. 3 (a)). The trapped air between the deck and water surface escapes from both ends of the deck, as the bubbles shown in Fig. 5 (b). Comparisons of wave-deck interaction simulated in the 2D and 3D CFD models are presented in Fig. 6, where the water volume fraction is represented by different colors (1 for water phase and 0 for air phase based on the VOF method). The wave profile of the 2D model is shown in Fig. 6 (a). The 2D model could not simulate the escape of the trapped air in the longitudinal direction (z direction), so the air is fully trapped beneath the deck. Thus, the 2D model underestimates the interaction area between wave and bridge, and the results could deviate from real values. On the other hand, the 3D model better simulates the flow of trapped air, as the green and red between deck and girders in Fig. 6 (b), representing the mixture of water and air phases. A top view of the 3D model is presented in Fig. 6 (c), from which we could better identify the airflow around the deck. In addition, the 3D CFD model simulates the wave-deck interaction at both ends of the model, which is closer to the experimental measurements, and thus could provide more reliable results. Comparisons between maximum vertical and horizontal wave forces (F_y and F_x) computed from 2D and 3D models are presented in Fig. 6 (d). As indicated, F_y computed from a 2D model are larger than those from a 3D model, while values of F_x are similar. This feature may be caused by the fact that waves and air cannot flow around the bridge in a 2D model (i.e., along the z or longitudinal direction), which could increase the pressure on the interaction surface. Generally, the 3D model could better solve the end effects, including the wave effects on the ends and the escape of trapped air, and could also simulate the complex wave-air-deck interaction for its spatial advantages.

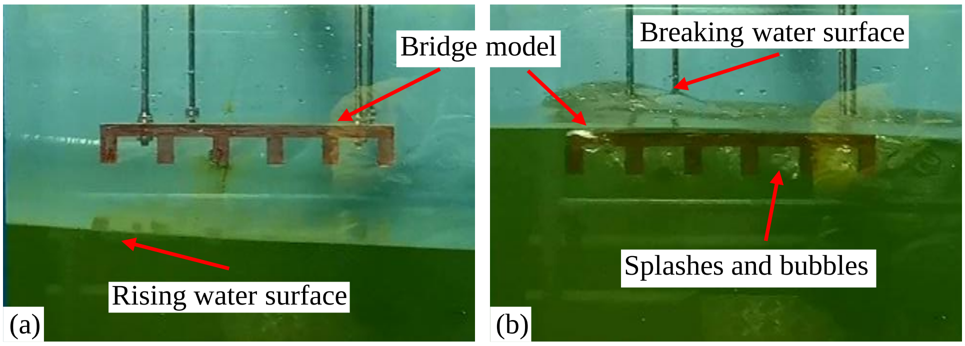

Fig. 5 Photos of the bridge model during the experiment

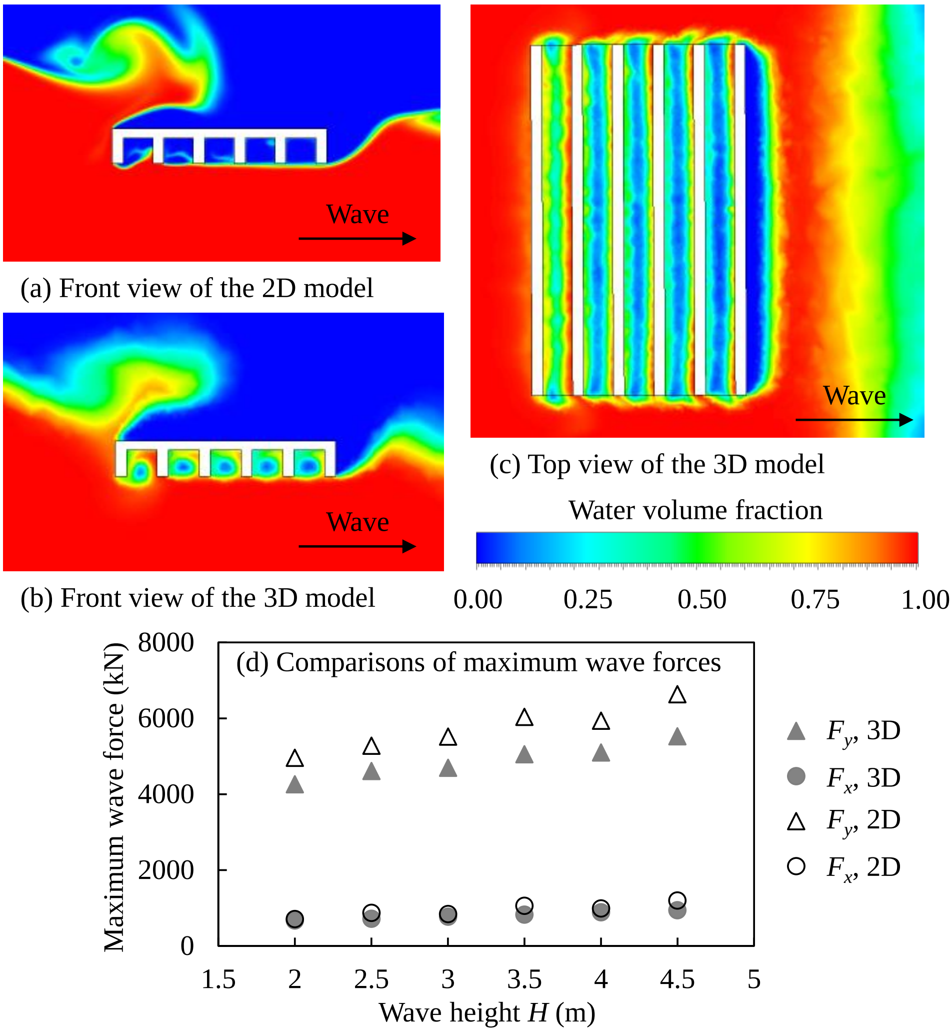

Fig. 6 Comparisons of wave-deck interactions and maximum wave forces in the 2D and 3D CFD models

To further validate the 3D model, comparisons of the wave force time histories between numerical results and experimental measurements, for a case with $D = 8.4$ m and $H = 3$ m in prototype scale ($D = 0.28$ m and $H = 0.1$ m in 1:30 laboratory scale), are shown in Fig. 7. The experimental measurements are converged to prototype scale according to the Froud scaling model. It should be noted that in all the following figures and discussions, the origin of time t does not necessarily refer to the actual starting point of the test wave, but for better presentation. As indicated, wave forces on the deck first reach the maximum value and then drop down to a trough. The vertical force has a larger magnitude as compared with horizontal force. Generally, there exist acceptable deviations between experimental and numerical results due to the scale conversion and measurement error, proving the accuracy of the established 3D CFD model.

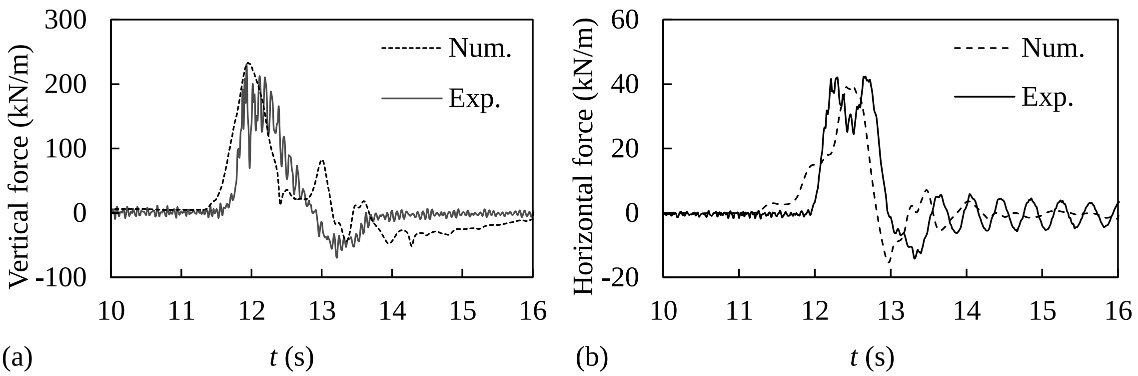

Fig. 7 Comparisons of wave force time histories between experimental and 3D CFD results

2.2 Properties of wave force using 3D CFD model

Schematic diagrams of different submerged conditions and bridge deck sections are illustrated in Fig 8. The unsubmerged condition is the case where the bridge deck is elevated from the water level before the wave arrives ($D \leq 10$ m). The partially submerged condition refers to the scenario where the surge water level reaches the bottom of the girder but not exceeds the top of the deck ($10 < D \leq 11.55$ m). For fully submerged cases, the surge water level is higher than the top of the deck ($D > 11.55$ m). To investigate the asymmetric wave force and structural responses, this study not only measures the overall wave force on the bridge deck but also the force on each section as indicated in Fig. 8. The investigation of wave force on each girder section can provide valuable information for the performance assessment of bearings under different scenarios, which could act as input for the overturning assessment of the bridge structure. The sections are numbered as 1 to 6 from the seaward to the landward side.

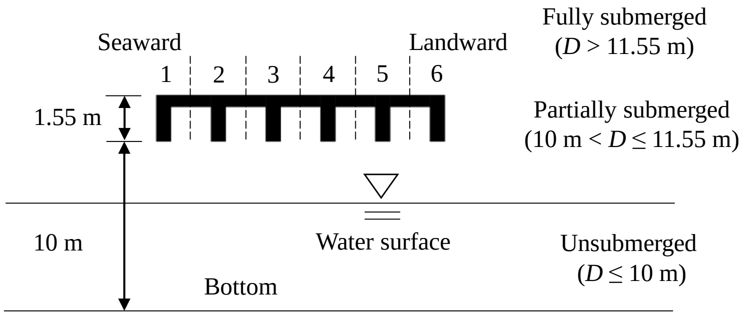

Fig. 8 Different submerged scenarios and investigated bridge sections

A typical case of the simulated wave-structure interaction in the 3D model is presented in Fig. 9. Four stages are illustrated: (a) initial stage; (b) water surface starts to rise; (c) wave overtops the bridge; and (d) after the wave. The pressure distributions on the bridge deck during this process are shown in Fig. 10 (in the bottom view for better illustration of the wave slamming effects). When the wave crest first overtops the bridge deck (*i.e.* Fig. 10 (c)), the total pressure is unevenly distributed on the bridge deck. Wave force concentrates on the seaward side, which would cause a large overturning moment on the deck and further lead to local component damage. Hence, it is vital to assess the influence of the extreme overturning moment when investigating structural performance.

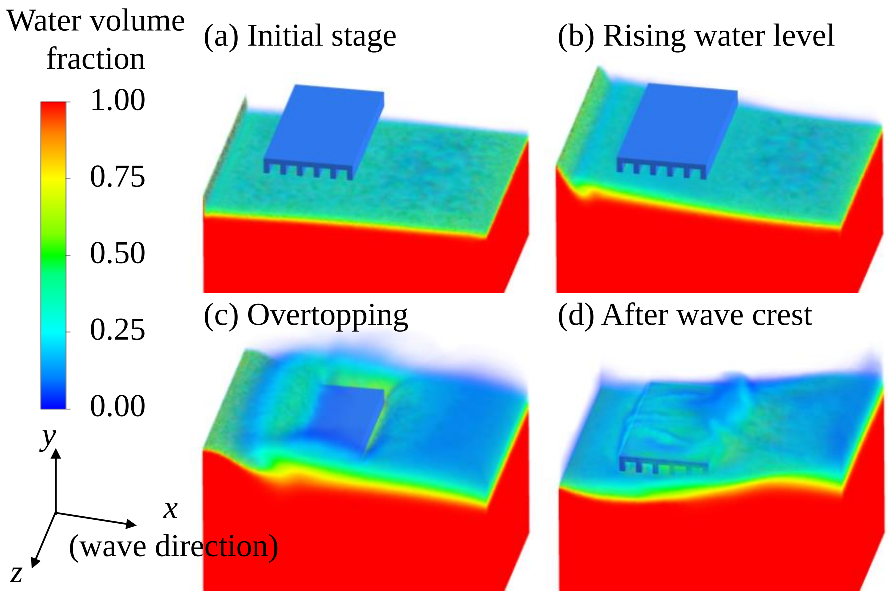

Fig. 9 Wave profiles simulated in the 3D numerical model

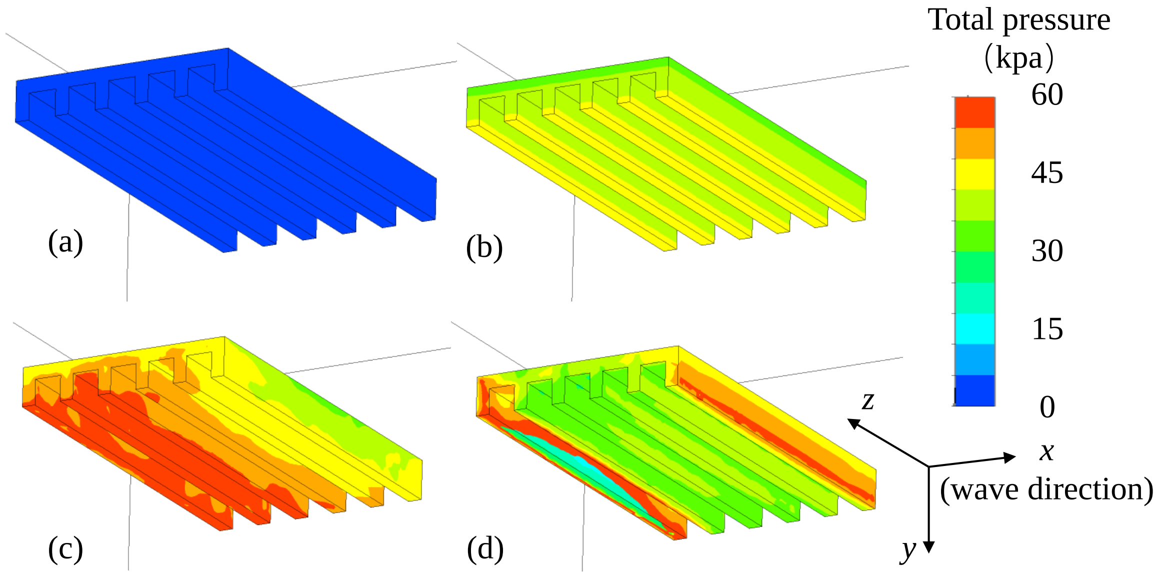

Fig. 10 Pressure distribution on the bridge considering the wave-structure interaction

The time series of the solitary wave force on each bridge section for a typical case with H = 4.6 m and D = 7 m are presented in Fig. 11. In this case, the bridge deck is elevated from the surge water level, but the wave is large enough to exceed the top of the deck. The vertical and horizontal wave forces on each bridge section (f_{yi} and f_{xi}) are shown in Figs. 11 (a) and (b), respectively. Positive values represent upward or forward forces (*i.e.* same direction as the wave flow), while negative values represent downward or backward forces (*i.e.* opposite direction as the wave flow). During the wave-structure interaction, f_{yi} and f_{xi} not only have different peak values but also reach their peaks at different moments. Peak vertical forces at the seaward side are larger than those at the landward side, while peak horizontal forces at the seaward side are smaller and f_{x6} is the largest one. These characteristics may be caused by the irregular shapes of the girders and the trapped air between the girders and the deck. The value of f_{yi} may be mainly contributed by the wave slamming impact, and hence gradually reduces as the wave progresses. In this process, the uplifting water surface is deformed and 'knocked' down by the deck and trapped air, and then pushed forward by the advancing wave. This part of deformed water could gather and increase as the wave moves forward, resulting in larger f_{xi} caused by the hydrostatic pressure. Generally, the maximum vertical force on each section of the deck f_{yi} decreases from seaward (f_{y1}) to landward side (f_{y6}), while f_{xi} is just the opposite.

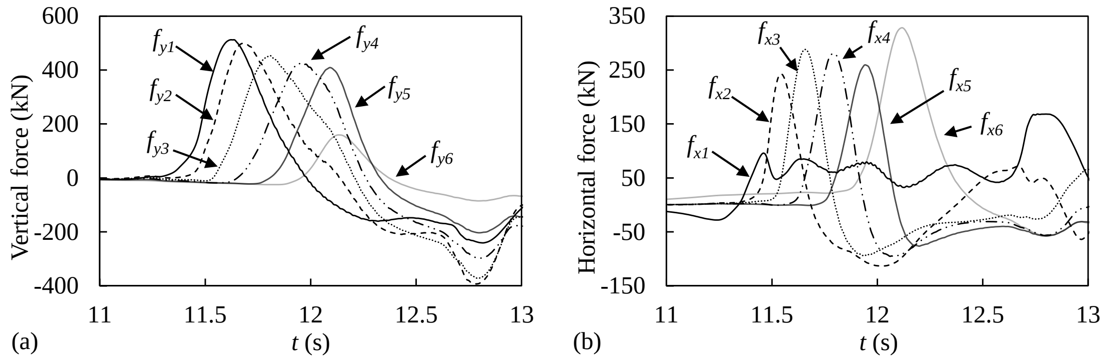

Fig. 11 Time series of wave forces on different bridge sections

The maximum vertical and horizontal wave forces on the whole bridge span (F_y and F_x) under different submerged scenarios are presented in Fig. 12, where the dimensionless parameter wave steepness H/λ is plotted along the x axis for the ease of comparison with the previous dimensionless study. Figs. 12 (a) and (b) show the results for the unsubmerged scenarios. F_y shows a close linear relationship with the wave steepness H/λ and the largest value occurs when $H/\lambda > 0.045$. Similarly, F_x increases linearly with H/λ and near-linearly with D. With respect to partially submerged scenarios as Figs. 12 (c) and (d), F_y changes little with H/λ, and decreases as D increases. F_x is larger than that for unsubmerged conditions, and is well fitted in a linear relationship with H/λ. For the fully submerged conditions shown in Figs. 12 (e) and (f), both F_y and F_x slightly increase for larger steepness, and gradually stabilize for D. Since the wave crest does not induce significant forces on the girder in fully submerged cases, F_y and F_x are much smaller as compared with other two scenarios. Generally, the wave-induced vertical and horizontal forces F_y and F_x vary and depend on different submerged scenarios, water depth D, and wave steepness H/λ. Wave forces show different characteristics under unsubmerged and fully submerged conditions, and those with respect to partially submerged cases could be seen as transitions between these two scenarios.

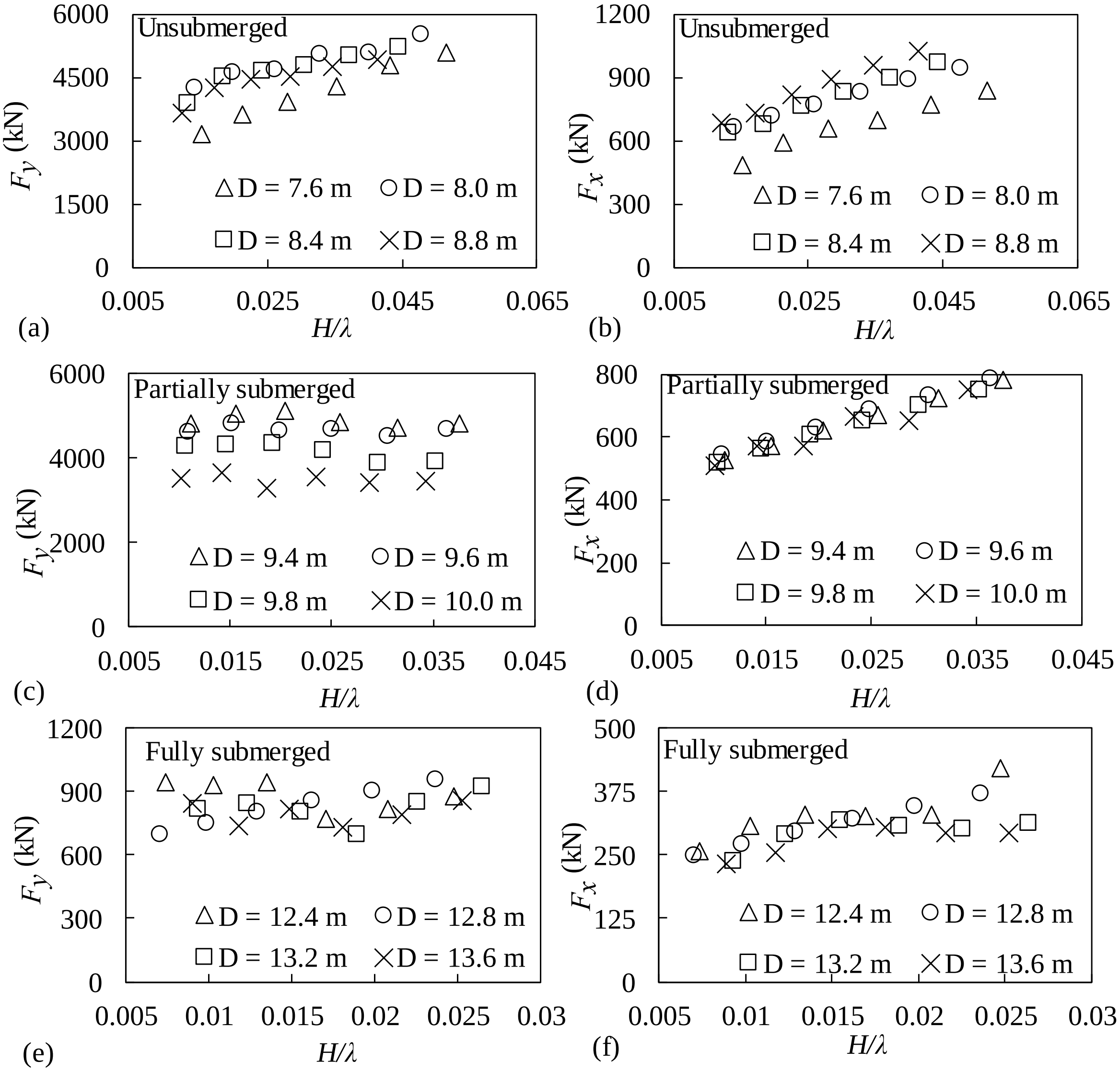

Fig. 12 Maximum vertical and horizontal wave forces under different submerged scenarios

3. Component-level analysis under wave forces based on 3D FEM

Solitary waves are simulated, and wave forces are computed using the 3D CFD model, while the complex loading and supporting conditions of the bridge could not be well solved in such a model. More specifically, the deck is constrained by multiple bearings with different constraint conditions, and their working states vary under the changing wave forces. Thus, a 3D FEM is adopted in this study for an accurate calculation of detailed structural responses, including overturning moment, bearing reaction force, and bearing performance. The model setups and results are introduced in this section.

3.1 FEM model setups

The 3D FEM is established by using the *ANSYS* Mechanical APDL package as shown in Fig. 13 (a). In this numerical model, SOLID 65 and COMBIN 39 (compression only) are used to simulate the concrete and constrain at each bearing, respectively. The ultimate concrete compressive strength $f_c^{'}$ is set as 37.1×10^6 N/m^2 and the axial tensile cracking stress $f_t^{'}$ is 3.25×10^6 N/m^2 [45]. The stress-strain relationship for the used concrete is defined as follows [45]:

$$\sigma_c = f_c^{'}\left[1-\left(1-\frac{\varepsilon_c}{\varepsilon_0}\right)^2\right] \qquad \varepsilon_c \le \varepsilon_0 \tag{3}$$

$$\sigma_c = f_c^{'} \qquad \varepsilon_0 \le \varepsilon_c \le \varepsilon_{cu} \tag{4}$$

where σ_c = concrete stress; ε_c = concrete strain; and ε_0 and ε_{cu} = peak and ultimate strains, which equal 0.002 and 0.0033, respectively. It is assumed that there is no descent stage considered for the concrete. Detailed material properties adopted in the model are listed in Table 1. The calculated weight of the bridge model is 1.36×10^5 N/m (2.15×10^3 kN per span).

Table 1 Material properties defined in the FEM

No.	Element	Material properties	
1	SOLID65	Concrete-(MISO)	
		Modulus of elasticity (EX)	3.524×10^{10} N/m^2
		Poisson's ratio (PRXY)	0.167
		Density	2600 kg/m^3
		Shear transfer coefficient for open crack	0.3
		Shear transfer coefficient for closed crack	0.5
		Axial tensile cracking stress	3.25×10^6 N/m^2
		Ultimate concrete compressive strength	37.1×10^6 N/m^2
2	COMBIN	Stiffness (compression only)	1.0×10^{10} N/m

The boundary conditions, *i.e.*, bearing constraints, of the model are determined based on practical engineering design. All the bearings are set as compression only in the vertical direction since generally the bearings are not designed to resist the uplift force [46], [47]. For the investigated simply supported bridge, the displacement in the longitudinal direction (z) is constrained at one end (*i.e.*, right side) of the span. Note that the longitudinal forces and rotation caused by longitudinal constraints are neglected in this model, which have a tiny influence on the results. In addition, bearings of the simply supported bridge are often designed to allow thermal movement caused by changing temperature, especially for hot and humid coastal regions [46], [48]. Thus, the constraints in the horizontal direction (x) are only set at bearing L3 and R3 at the two ends of the span. Details of the boundary conditions are listed in Table 2.

Based on the 3D CFD numerical model, the vertical wave forces mainly act on the deck, while the horizontal forces mainly act on girders. Therefore, the wave forces obtained from the CFD model are applied on the bridge along the longitudinal direction as Fig. 13 (b). The applied wave loads are constant forces determined by tracing the wave force time series and selecting values of several most unfavorable moments, *e.g.*, when the overall wave force on the bridge span reaches the peak value and when the wave force on certain section(s) (as Fig. 8) reaches the maximum. The overturning moment is calculated by accumulating the contribution of each force component as indicated in Fig. 13 (b). The reference point of the overturning moment O is set at the bottom of the landward girder (girder 6), which is consistent with the simulated overturning results and in line with guide specifications [49]. The horizontal moment arm L_{Fhi} equals half of the girder height, while the vertical moment arm L_{Fvi} depends on the horizontal projection to center O.

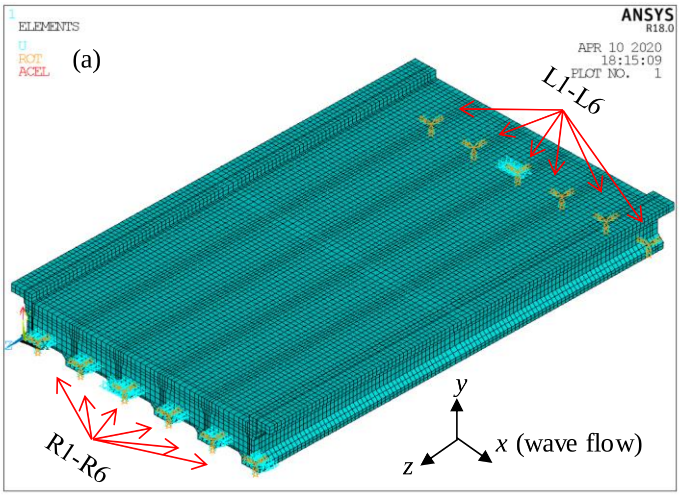

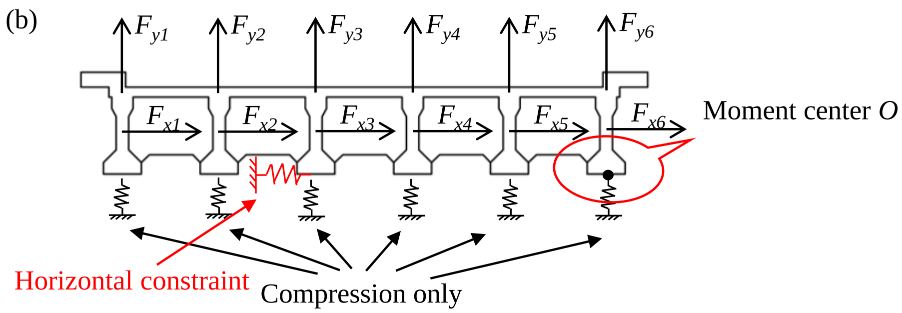

Fig. 13 (a) FEM bridge model and (b) illustration of the boundary conditions and overturning moment center

Table 2 Setups of the constraints associated with the bearings

No.	Horizontal (*x*)	Vertical (*y*)	Longitudinal (*z*)
R1	-	C_O	Constraint
R2	-	C_O	Constraint
R3	Constraint	C_O	Constraint
R4	-	C_O	Constraint
R5	-	C_O	Constraint
R6	-	C_O	Constraint
L1	-	C_O	-
L2	-	C_O	-
L3	Constraint	C_O	-
L4	-	C_O	-
L5	-	C_O	-
L6	-	C_O	-

Note: Constraint represents the bearing cannot move along the corresponding direction, - means no constraint in the corresponding direction, and C_O refers to the bearings with the property of compression only. For a simply supported bridge, displacement in the longitudinal direction (*z*) is constrained at the right end of the bridge. Furthermore, only one constraint is set at each end of the bridge to release the concrete temperature effect in the horizontal direction (*x*). More specifically, only R3 and L3 cannot move in the horizontal direction (*x*).

3.2 Bearing working state and reaction force

Given the relevant parameters used in the FEM, the peak overturning moments, corresponding bearing reaction forces, and working states are presented in Fig. 14. The positive value represents compressed (normal) working state, while a zero value refers to the disengaged state since there is no tension (negative value) from compression-only bearings. Disengaged bearing no longer provides constraint and is considered a component failure. Due to the different constraints at L and R sides, two bearings connecting to the same girder could have different performances.

Fig. 14 (a) shows the case where the peak overturning moment M = 3023 kN×m, which is relatively small as compared with the capacity from the deck weight. All the bearings are working properly. Reaction forces and working states of bearings at seaward and landward sides gradually vary for larger M as indicated in Fig. 14 (b). L1 and L2 are disengaged, and R1 and R2 are also close to the limit state. With M further increases, more bearings are damaged, and the deck weight is concentrated on L6 and R6 as shown in Fig. 14 (c). Horizontal constraints provided by the bearings are significantly reduced in this case, expediting the failure of the deck. Fig. 14 (d) presents the results for M = 12067 kN×m, where most of the bearings are damaged, and only L6 and R6 still work. It is difficult for two bearings to maintain structural stability and the deck could be easily washed away.

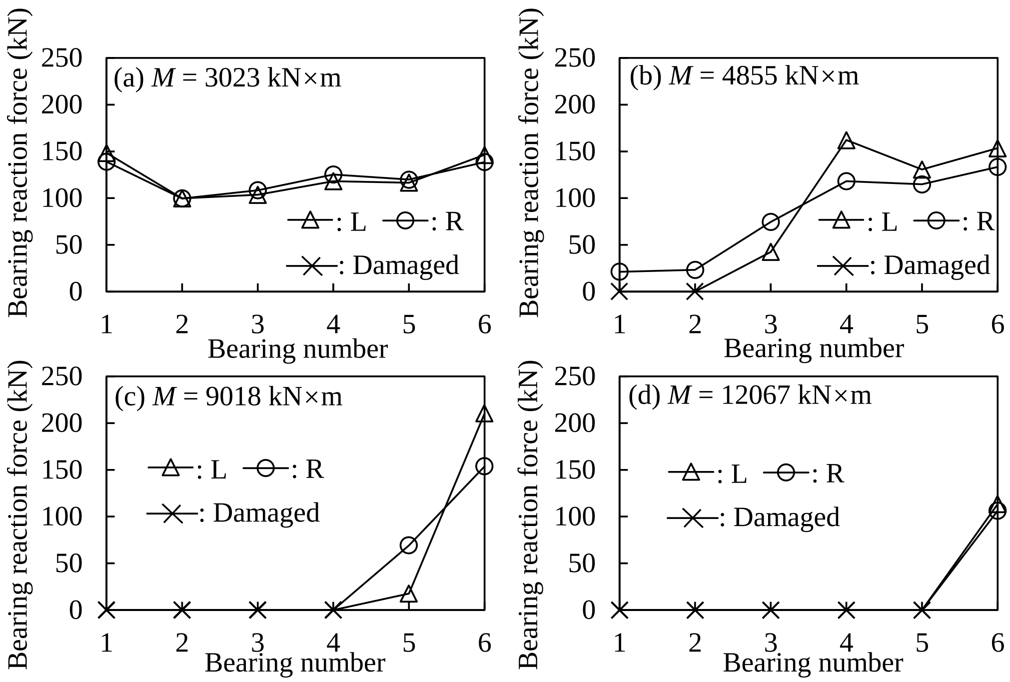

Fig. 14 Bearing reaction forces and performance

3.3 Overturning moment under different wave scenarios

The peak overturning moment considering bearing performance is calculated with FEM as well. Similarly, M shows different characteristics under different submerged scenarios, and typical results are presented in Fig. 15. For unsubmerged cases, M increases for larger H/λ, but is less affected by water depth D. The maximum value occurs when H/λ is larger than 0.05. On the other hand, M has no obvious monotonic relationship with H/λ under fully submerged conditions. It tends to reduce as D increases. Generally, peak overturning moments in unsubmerged cases are larger than those in fully submerged cases. The extreme overturning moment could destroy seaward bearings first, and the changed constraints would further affect the structural stability, causing the bridge deck to overturn.

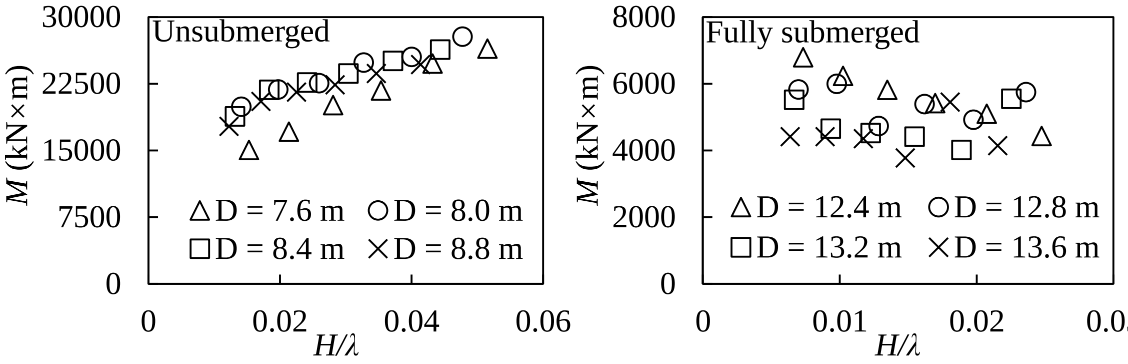

Fig. 15 Overturning moment under different submerged scenarios

4. Proposed novel component-level overturning failure mode

Based on the numerical and experimental investigations on the wave-structure interaction, a novel component-level overturning failure mode is proposed considering the wave-induced overturning moment, bearing working state, and reaction force. Damage states are defined, and criteria are computed using 3D FEM.

4.1 Comparison of the overturning and unseating failure modes

The primary failure mode of the coastal bridge under hurricane considered in previous studies is the deck unseating by comparing the maximum wave force F_y with the deck capacity [2].

Once F_y exceeds the sum of deck weight W_s, the deck is considered as a failure. Although this model could describe some damaged bridges during hurricane events, it does not account for wave force distribution, bearing performance, and overturning moment. Moreover, the overturning failure mode could be more critical, since a small but concentrated load could cause component damage, expediting deck failure.

Component damage refers to the damage of bearings herein. Once the compression-only bearing is disengaged by the uplift force, the bearing is considered damaged. Comparisons of the deck overturning and unseating failure modes are presented in Fig. 16 for a typical case where the surge water depth D is 7 m (clearance $Z_c = 3$ m). As indicated, the peak vertical force F_y is relatively small as compared with the deck weight W_s, and the limit state (the gray line) has not been reached. However, component damage occurs due to the overturning effects. The extreme overturning moment leads to bearing failure when $H > 3.4$ m, and more bearings are destructed for larger wave height and overturning moment. Since the unseating failure mode is considered by comparing total wave force on the bridge deck with the deck weight, it fails to identify the loading condition and damage of local bearings, which may overestimate the overall capacity of the bridge.

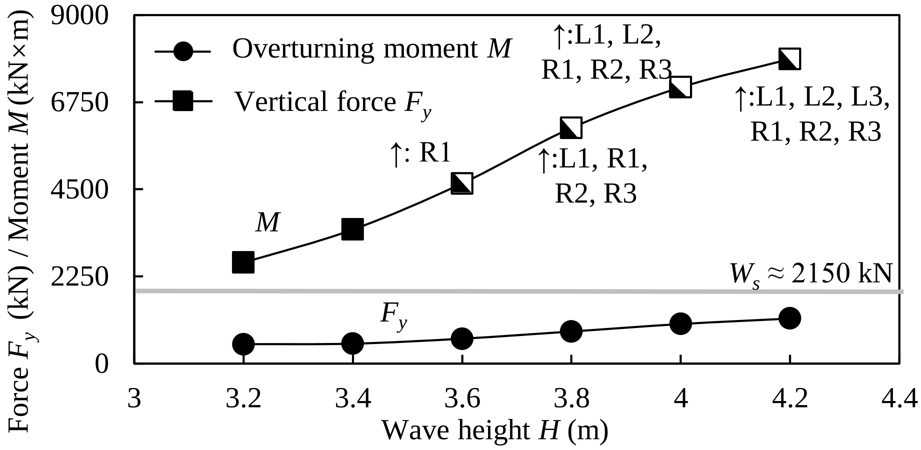

Note: ↑ refers to damaged bearings. Half-filled symbols indicates component damage cases.

Fig. 16 Comparisons of overturning and unseating effects

4.2 Limit states by considering overturning failure mode

For clear clarification of the relationship within bearing damage, overturning effects, and deck failure, four limit states are defined by tracing the CFD and FEM simulations for the investigated bridge as:

- Level 1: No damage;
- Level 2: Slight damage, where component damage occurs;
- Level 3: Moderate damage, where the constraint is severely reduced; and
- Level 4: Extensive damage, where deck failure occurs.

An uplift line load is applied at the seaward girder (connecting bearings L1 and R1) in the 3D FEM, and the overturning moment, bearing reaction force, and bearing performance are computed. The applied load is proportionally increased (amplified) until the final failure or calculation divergence. The overturning moment M and corresponding bearing reaction forces f_{Li} and f_{Ri} are recorded and presented in Fig. 17. Every time a bearing is disengaged (reaction force becomes 0), the bridge constraints and the reaction forces of the residual bearings would change. Fig. 17 (a) shows the results for seaward bearings which would be destroyed earlier. At the initial state without external overturning moment, the weight of the bridge deck is evenly distributed on each bearing, which means the extension lines of each segment on the left side will converge at the same point. As indicated, bearing R1 is the first to be disengaged, indicating the bridge reaches the component damage Level 2. The limit overturning moment at this state is 3746 kN×m. With M further increases, multiple bearings are damaged in turn including L1, R2, and L2. When M reaches 6368 kN×m, bearing R3 damages, which means the deck loses x-direction-constraint at R side. This state is determined as the Level 3 limit state for the investigated bridge, since unacceptable and nonreversible movement may generate in this state due to insufficient constraint in the x direction. Level 4 limit state is defined as when bearing L3 is disengaged (7696 kN×m). At this state, both bearings providing constraints in the x direction (L3 and R3) are destroyed, and the deck could be washed away laterally. Results for landward bearings are illustrated in Fig. 17 (b). Although the failure limit states of these bearings are larger than the Level 4 limit state, the remaining bearings are not enough to provide sufficient constraints.

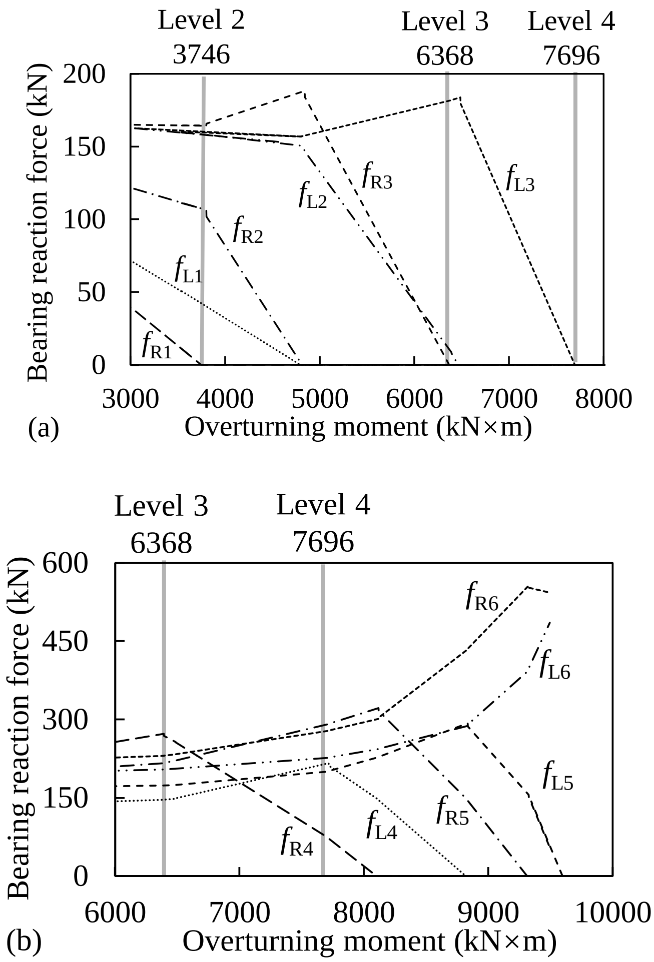

Fig. 17 Limit states, bearing reaction forces, and external overturning moments

For a better illustration, the vertical displacements of the bridge deck at each limit state are presented in Fig. 18. The downward deformation is represented by blue, and the uplifted part caused by the wave force is presented in red and yellow. Destructive bearings at each damage level are marked with arrows. No damage Level 1 is shown in Fig. 18 (a). Two ends of the deck are supported by bearings and the middle section is downward because of the deck weight. No bearing disengagement or component damage occurs at this stage. At Level 2 limit state as shown in Fig. 18 (b), the downward deformation at the seaward side is reduced by uplift force. Then, multiple bearings are damaged at Level 3 and Level 4 limit states as Figs. 18 (c) and (d), respectively. The uneven force and displacement distributions not only exist on the seaward and landward sides, but also on the L and R sides. The new overturning failure mode not only provides more critical limit states but also comprehensively considers deck and component spatial performances, facilitating the reliability analyses of coastal bridges.

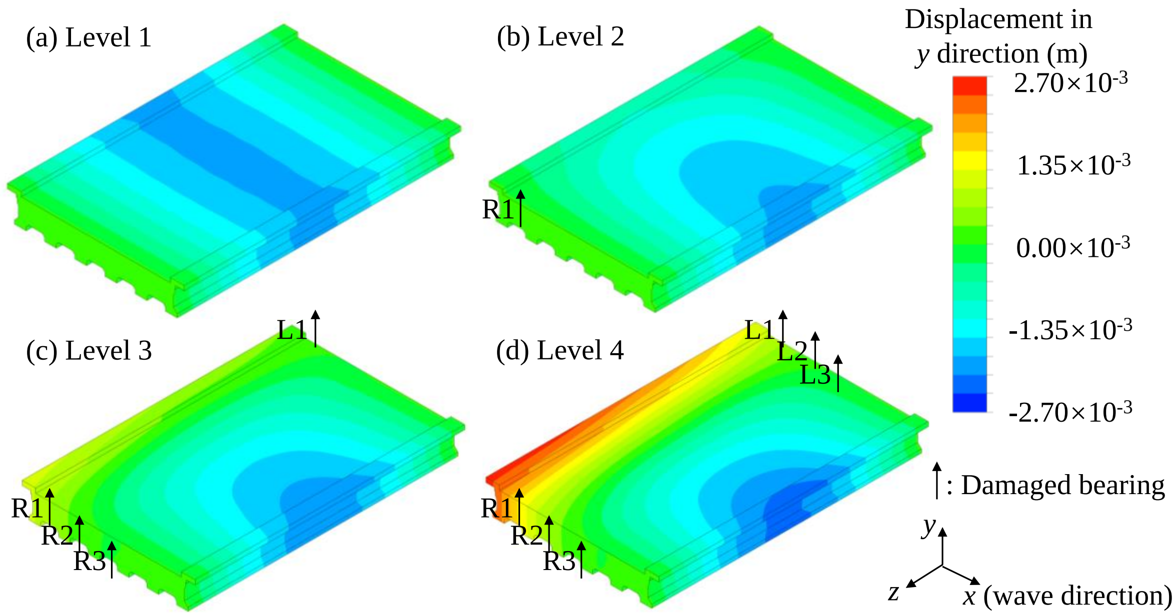

Fig. 18 Displacement of the deck and bearings at different limit states

5. Vulnerability analyses based on new failure mode

5.1 Surrogate models for peak wave force and overturning moment

In order to reduce the high computational expense of the 3D numerical model, surrogate models are examined to quantify the peak wave force and overturning. The 3D simulation could provide reliable and detailed results as introduced previously but may be limited to its high computational cost, especially for probabilistic performance assessment which requires a large amount of calculation. Based on typical calculation results, the general function between the structural responses and the wave parameters could be summarized. After verification of its prediction accuracy through mathematical methods, such a function (*i.e.*, surrogate model) could be utilized to calculate the general structural responses. The experimentally verified 3D numerical model also ensures the credibility of the data source for the surrogate model.

After several calculations and comparisons, the polynomial surface model with stepwise regression method [50] is employed, which has also been adopted in several engineering studies [51]. The general equation is

$$y' = \theta_0 + \sum_{i=1}^{q} \theta_i m_i + \sum_{i=1}^{q} \sum_{j=1}^{q} \theta_{ij} m_i m_j \tag{5}$$

where y' = the approximating function; m_i and m_j = the model predictors such as wave height and wavelength; θ_i and θ_{ij} = the model parameters; and q = the number of total predictors considered in the model.

A total of 389 datasets (168 for the unsubmerged conditions, 84 for the partially submerged conditions, and 137 for the fully submerged conditions) from the numerical analysis are used within the surrogate model. The 5-fold cross-validation method is utilized to evaluate the predictive performance of the surrogate model. The original sample (*i.e.*, structural responses computed from the numerical model) is randomly partitioned into 5 equal-sized subsamples, and one single subsample is retained to validate the model trained from the other 4 subsamples. The cross-validation process is repeated for each subsample, and the coefficient of determination (R^2) and the normalized root-mean-square error (NRMSE) are adopted as the goodness-of-predict, which are calculated as

$$R^2 = 1 - \frac{\sum_{i=1}^{q} \left(y_i - y_i' \right)^2}{\sum_{i=1}^{q} \left(y_i - y_{\text{mean}} \right)^2} \tag{6}$$

$$\text{NRMSE} = \frac{\text{RMSE}}{y_{\max} - y_{\min}} = \frac{\sqrt{\sum_{i=1}^{q} \frac{\left(y_i - y_i' \right)^2}{n}}}{y_{\max} - y_{\min}} \tag{7}$$

where y' and y = predicted values and observed values respectively; y_{mean} = the mean value of the samples; and $y_{\max}$ and $y_{\min}$ = the maximum and minimum sample in each subsample, respectively. Small NRMSE value indicates good prediction performance of the surrogate model.

Since the characteristics of the wave forces and structural responses vary for different submerged scenarios, different predictors are determined for each scenario. For the unsubmerged cases, the wave forces are quantified with clearance Z_c and wave height H as

$$F' = \theta_0 + \theta_1 Z_c + \theta_2 H + \theta_{11} \left(Z_c \right)^2 + \theta_{12} H Z_c + \theta_{22} H^2 \tag{8}$$

The fitting coefficients and NRMSE values are listed in Table 3.

Table 3 Fitting coefficients for unsubmerged cases

	NRMSE	R^2	θ_0	θ_1	θ_2	θ_{11}	θ_{12}	θ_{22}
F_y	0.059	0.929	3515	1851	-324.9	-1053	51.57	148.4
F_x	0.056	0.910	318.3	-14.24	178.6	-77.72	21.92	-8.23
M	0.048	0.918	13690	5979	1505	-4723	837	181.5

For the partially submerged cases, the wave forces are quantified with wave steepness H/λ and initial trapped air ratio A_r, accounting for both the various water depths and the trapped air quantity as

$$F' = \theta_0 + \theta_1\left(\frac{H}{\lambda}\right) + \theta_2 A_r + \theta_{11}\left(\frac{H}{\lambda}\right)^2 + \theta_{12}\left(\frac{H}{\lambda}\right)A_r + \theta_{22}A_r^2 \tag{9}$$

$$A_r = \frac{C_d + d_g - D}{d_g} \tag{10}$$

where C_d = design clearance and d_g = girder height. The relative coefficients are listed in Table 4.

Table 4 Fitting coefficients for partially submerged cases

	NRMSE	R^2	θ_0	θ_1	θ_2	θ_{11}	θ_{12}	θ_{22}
F_y	0.093	0.922	3036	3662	5047	98910	19510	-2886
F_x	0.038	0.984	367.6	13150	89.96	-83620	258	-95.03
M	0.089	0.902	13630	45760	21190	65170	98000	-12600

For fully submerged cases, the wave force is mainly affected by the submerged ratio, and changes little with wave height and steepness. Wavelength λ and submerged ratio M_r are determined as the predictors as:

$$F' = \theta_0 + \theta_1\lambda + \theta_2 M_r + \theta_{11}\lambda^2 + \theta_{12}\lambda M_r + \theta_{22}M_r^2 \tag{11}$$

$$M_r = \frac{-(C_d - S)}{d_b + d_g} \tag{12}$$

where d_b = deck thickness and S = surge height.

Table 5 Fitting coefficients for fully submerged cases

	NRMSE	R^2	θ_0	θ_1	θ_2	θ_{11}	θ_{12}	θ_{22}
F_y	0.106	0.851	4289	-7.671	-2120	0.0257	-1.699	497.3
F_x	0.058	0.942	1050	-1.754	-317.6	0.001961	-0.0204	54.7
M	0.099	0.887	12650	7.561	-5460	-0.01727	2.834	615

5.2 Probabilistic vulnerability analysis

Comprehensively considering the unseating failure mode and the overturning failure mode, the limit state function is developed as

$$P(F) = P\left[G_F\left(C_F, D_F\right) \leq 0 \text{ or } G_M\left(C_M, D_M\right) \leq 0 \middle| IM\right] \tag{13}$$

where G = the limit state function; C_i = structural capacity; D_i = structural demand; $P(F)$ = the probability failure of the bridge span; IM = the hazard intensity measure; and the subscript F and M represent unseating and overturning failure mode, respectively.

The structural demand D_F and D_M, which are the peak vertical wave force and overturning moment on the bridge deck under a certain wave, could be derived from the surrogate model results as introduced previously. With respect to the overturning failure mode, the structural capacity C_M for the 4 limit states are 0, 3746, 6368, and 7696 kN×m, respectively (as Fig. 17). The capacity C_F for the unseating failure mode can be calculated as [5]

$$C_F = W_s = \left(d_b W + A_g n_g\right)\gamma l \tag{14}$$

where W_s = the static weight of the deck; W = the deck width; A_g = cross-sectional area of girders; n_g = girder number; γ = unit weight of the deck; and l = span length.

The experimental and numerical based methods provide deterministic estimates of surge and wave impacts, which may yield conservative estimations for undetermined wave uncertainties. The probabilistic distributions employed variables are introduced as follows. A classic Rayleigh distribution [52] is adopted to model wave heights during a hurricane, which has been examined by several studies with measured data including [53], [54]. The probability density function (PDF) is as

$$f_H(h) = \frac{h}{H_{\mathrm{mode}}^2} \exp\left(-\frac{h^2}{2H_{\mathrm{mode}}^2} \right) \tag{15}$$

$$H_{\mathrm{mode}} = \frac{1}{2} H_s \tag{16}$$

where H_{mode} = the mode wave height and H_s = the significant wave height, which equals the mean wave height of the highest third of the waves in an event.

The surge height distribution during a hurricane is hard to predict because of the large number of meteorological and environmental factors involved. [55] used the Freund bivariate exponential distribution to represent the joint distribution of rainfall intensities and the corresponding storm surges. [56] proposed a Gumbel logistic model for representing a multivariate storm event. [57] utilized the Logistic correlation model to correlate the extreme surge and waves. However, these methods lack data support due to field measurement difficulties. Herein, a uniform distribution ranging ± 20% is utilized for the surge height [25].

Uncertainties in the unit weight of construction materials, workmanship error, and construction error are considered in the capacity modeling. A uniform distribution with lower and upper limits of 95 and 105% is used to account for workmanship and construction errors in deck thickness. A normal distribution for concrete and steel density is used in this study according to [58]. The mean density for concrete is taken as 2,600 kg/m^3, with a coefficient of variation (COV) of 0.04. For steel, the mean density is 7,850 kg/m^3 and COV is 0.01. The calculated bridge deck density also follows a normal distribution with a mean of 2.2×10^5 kg/m^3 and a COV of 0.036. Similarly, the overturning capacity at each limit state is considered as normally distributed with a COV of 0.04. Table 6 lists the main hurricane hazard parameters with respect to demand modeling.

Table 6 Hurricane hazard parameters used in reliability analysis

Hurricane hazard parameters	
Wave height H	Rayleigh distribution
Surge height S	Uniform distribution
Surge water depth D	Function of S

Wavelength λ	Determined by applied wave theory
Wave steepness H/λ	Function of H and λ
Initial air ratio A_r	Function of C_d, d_g, and D
Submerged ratio M_r	Function of C_d, d_g, d_b, and S

5.3 Reliability analysis and fragility surface

With the probabilistic vulnerability model proposed above, the fragility surface could be calculated by performing 1,000,000 Monte-Carlo simulations for each combination of *IM*s. The fragility surface intuitively displays the bridge failure probability under a certain intensity measure. A fragility surface of exceeding the Level 4 limit state for the investigated bridge is presented in Fig, 19 (a). A sharp increase in the failure probability is observed when S is around 2 - 3 m, which corresponds to a category 2 or 3 hurricane based on the Saffir-Simpson Hurricane Wind Scale (SSHWS). This method defines hurricane scale with several parameters, including wind speed, surge height, air pressure, and wave height, *etc*., and the wind speed U and surge height S are adopted in this study. After $S > 3$ m, the bridge span is under a relatively higher failure probability due to the large surge water depth. Generally, the failure probability is more sensitive to the value of S than H_s.

The bridge failure probability for a certain hurricane category (classified by wind speed) could be estimated by determining the relationship of maximum hurricane wind speed $U_{\max}$ with H_s and S. The significant wave height during a hurricane event can be calculated as [59]

$$H_s = 5.112 \times 10^{-4} U_A F^{1/2} \tag{17}$$

$$U_A = 0.71 U_{\max}^{1.23} \tag{18}$$

where U_A = the wind stress factor; F = the fetch length, which is treated deterministically as 5000 m; and $U_{\max}$ = the maximum hurricane wind speed. The surge height S is taken as a linear function with $U_{\max}$ [60], [61]. The exceeding probability of different overturning limit states as well as the unseating failure mode are plotted in Fig. 19 (b), and the regions for each hurricane category are highlighted as well. It is observed that the bridge is under relatively small failure probability under a category 1 hurricane, and the failure probability sharply increases for hurricanes over category 2 due to the increasing surge and wave heights. The unseating failure mode underestimates the failure probability of coastal bridges during hurricane events.

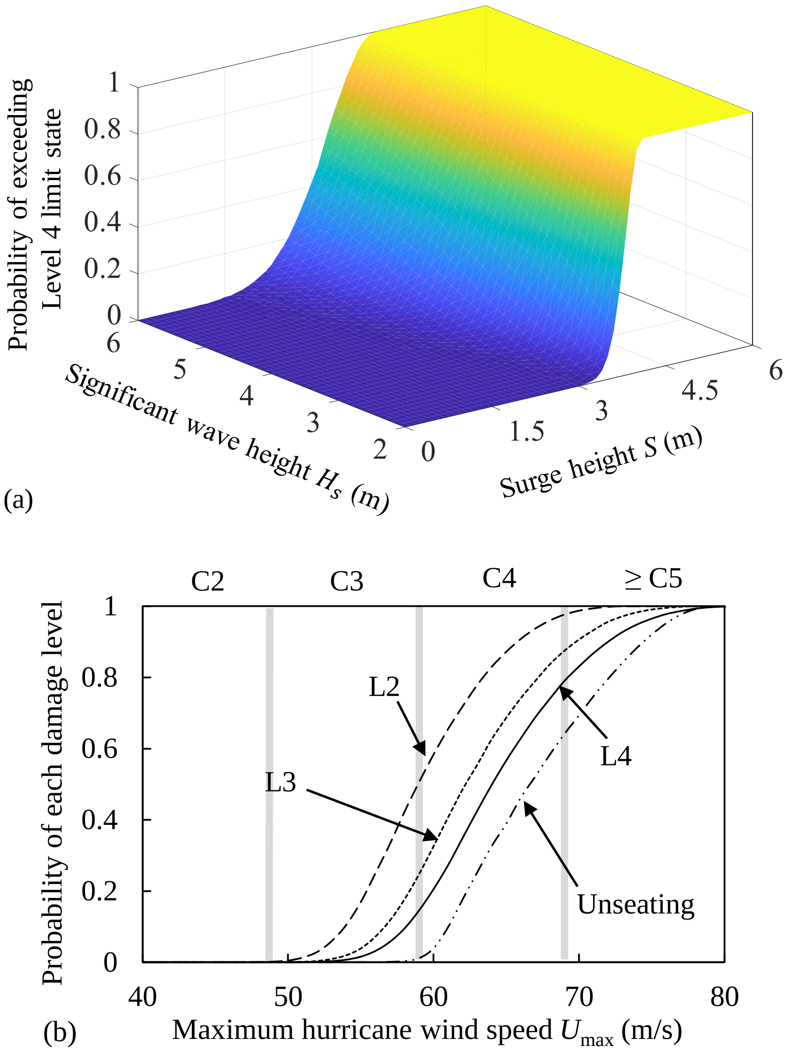

Fig. 19 (a) Fragility surface under surge and wave conditions and (b) Failure probability associated with different damage levels under specific hurricane intensities

5.4 Long-term failure probability and climate change effects

The long-term failure probability is calculated by accumulating the product of hurricane occurrence rate and corresponding bridge failure probability. Changing hurricane wind speed could affect the coastal environment and wave scale, which further contributes to the deck-wave interaction and structural responses. Several studies utilized annual wind speed distribution over an area as the hurricane occurrence model. For instance, [62], [63] modeled the hurricane wind speed in a given year as a Weibull distribution based on the annual wind speed meteorological data. Such a method could describe the annual weather of a region but may not be suitable for extreme events such as a hurricane. Therefore, this study adopts the method of the probability distribution of the maximum wind speed during a hurricane event to assess the hurricane failure probability [64]. Accordingly, a two-parameter Weibull distribution of the maximum hurricane wind speed during each hurricane is used to simulate the probabilistic wind speed, and a Poisson point process model is utilized as the hurricane occurrence model within the investigated time interval. Accordingly, the cumulative density function (CDF) of the maximum wind speed during hurricane events F_U, and the CDF of maximum wind speed during [0, T] period F_r are given by

$$F_U(u) = 1 - \exp\left[-\left(\frac{u}{\alpha}\right)^{\beta}\right] \tag{19}$$

$$F_r(u) = \exp\left[-\omega T\left(1 - F_U(u)\right)\right] \tag{20}$$

where u = wind speed; α and β = two parameters sorted from the weather record data; T = the investigated time interval in year; and ω = the mean annual occurrence rate of the hurricane.

Furthermore, to describe the effects of climate change on the long-term hurricane hazard model, the shape parameter β is assumed unchanged, while the hurricane occurrence rate ω and the maximum wind scale parameter α are time-variant [58]

$$\omega(t) = \omega_0 + r_\omega t \tag{21}$$

$$\alpha(t) = \alpha_0 + r_\alpha t \tag{22}$$

where r_ω and r_a = the annual increment rate in hurricane occurrence rate and maximum wind speed, respectively. The parameters ω_0, α_0, and β are 0.245, 35.9, and 2.06, respectively based on historical data obtained from US National Oceanic and Atmospheric Administration [37].

Based on previous research on climate change effects [33], [35], an 10% increment rate during 50 years for both $\omega(t)$ and $\alpha(t)$ is assumed in this study, and the CDF curves of the maximum hurricane wind speed during a period (T) of 30, 50, 70 and 100 years with and without considering the climate change effects are plotted in Figs. 20 (a) and (b), respectively.

In Fig. 20, the point on the curve represents the probability of the maximum wind speed resulting from the hurricanes not exceeding a certain value. Given the CDF, the probability density function (PDF) can be easily obtained to determine the occurrence probability of the relevant maximum wind speed within hurricanes. The curve on the right side of the figure means that a large-scale hurricane (with a large maximum wind speed) is more likely to occur within the investigated period. It could be found by comparing Figs 20 (a) with (b) that, considering the impact of climate change, the occurrence probability of extreme wind speed resulting from hurricanes would become larger under a longer investigated period. The failure probabilities (e.g., probability of exceeding the damage level) within the investigated time interval under different scenarios are listed in Table 7. Results from the unseating failure mode without considering the overturning effects are calculated as well, and the climate change effects are examined and compared. The failure probability remarkably increases for a longer estimation period, especially for Level 3 and Level 4 limit states (from 0.3743 to 0.9331 and 0.3301 to 0.9008, respectively). The 100-yr period has the highest bridge failure probabilities of 0.9639, 0.9331, and 0.9008 due to the cumulative effect of the time period. Neglecting the overturning effect could result in underestimation of bridge failure probability by 5 - 15% based on different time intervals.

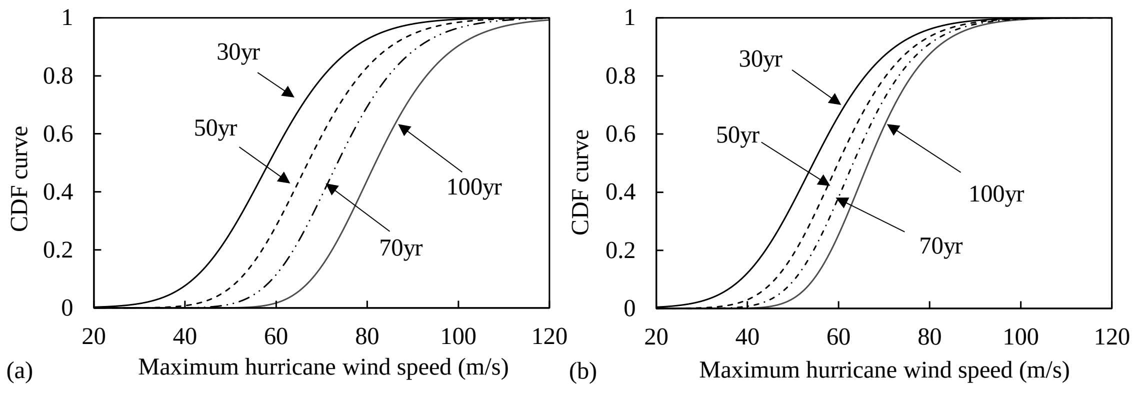

Fig. 20 CDF curves of maximum hurricane wind speed under different time periods (a) with considering climate change effects and (b) without considering climate change effects

Table 7 Probability of failure within the investigated period

		30 yr	50 yr	70 yr	100 yr
With CM effects	Level 2	0.4618	0.7093	0.8667	0.9639
	Level 3	0.3743	0.6138	0.7932	0.9331
	Level 4	0.3301	0.5600	0.7463	0.9008
	Unseating	0.2692	0.4830	0.6767	0.8708
No CM effects	Level 2	0.3511	0.5050	0.6174	0.7340
	Level 3	0.2719	0.4032	0.5063	0.6225
	Level 4	0.2340	0.3520	0.4476	0.5594
	Unseating	0.1827	0.2814	0.3654	0.4691

Apparently, climate change could significantly increase the bridge failure probability as listed in Table 7. For a better understanding of such phenomenon, a sensitivity analysis is performed by using different time-variant hurricane scale parameter $\alpha(t)$ and occurrence rate $\omega(t)$ as shown in Fig. 21. Increment rates of 0%, 5%, 8%, 10% during a 50-year interval [35] are examined for both $\alpha(t)$ and $\omega(t)$. The relative failure probability is calculated as the ratio of Level 4 failure probability under each climate change scenario to that calculated without considering climate change effects (*i.e.*, 0% for both $\alpha(t)$ and $\omega(t)$). As indicated, the bridge failure probability could increase by 40% during a 30-year period (relative failure probability equals 1.4), while which could be over 90% for a 100-year period (relative failure probability exceeds 1.9). Bridge with longer service life would suffer more from the climate change effects. The increment in $\alpha(t)$ has a greater impact on the failure probability as compared with $\omega(t)$ since it directly affects multiple demand parameters including surge and wave heights.

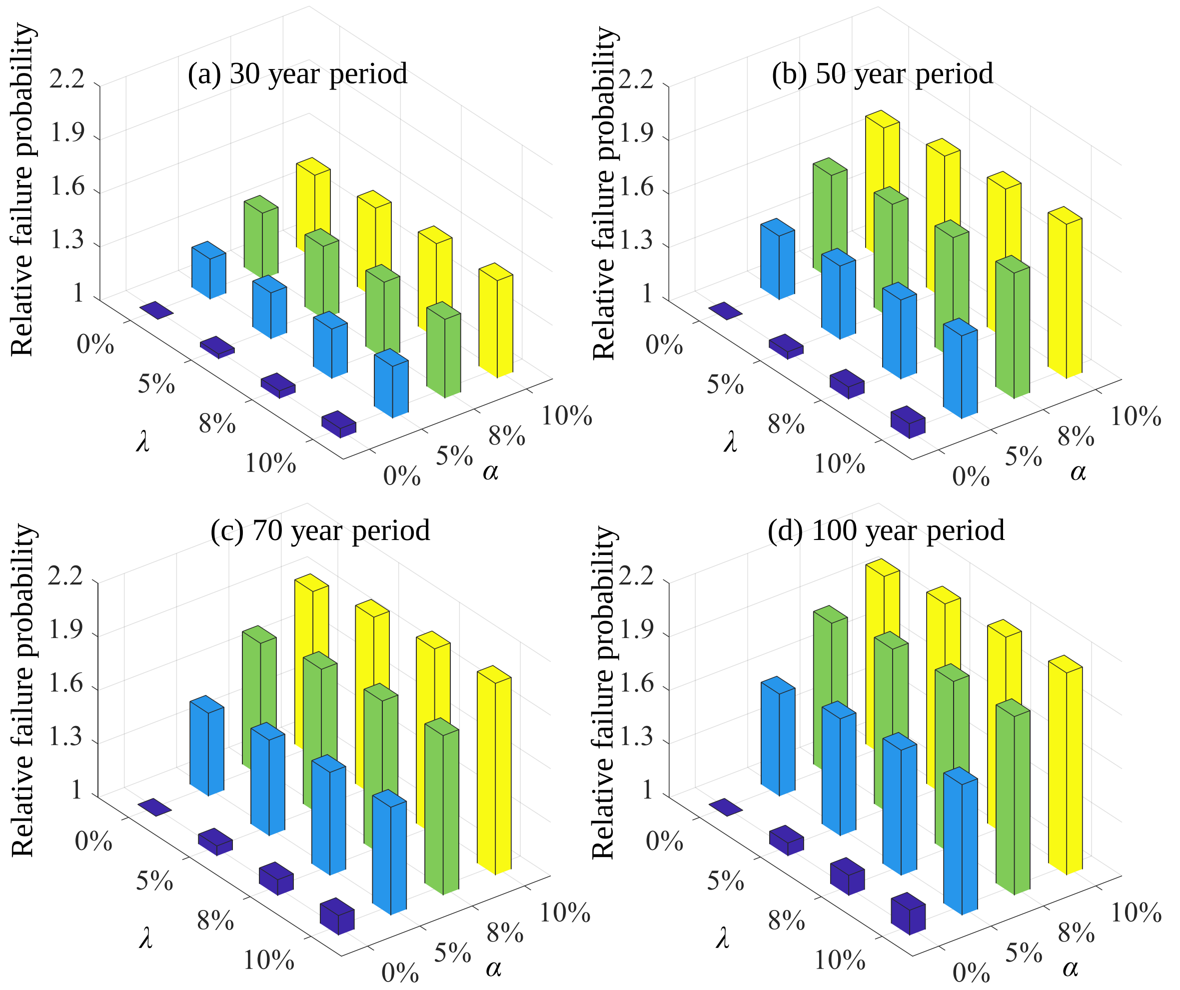

Note: λ and α refer to an increment rate per 50 years for hurricane occurrence rate and maximum hurricane wind scale, respectively. The relative failure risk is calculated as the ratio of Level 4 failure risk under each CM scenario over the initial risk without CM effects (i.e. 0% for both λ and α)

Fig. 21 Sensitivity analysis of climate change effects on long-term failure probability

6. Conclusions

This study focuses on the performance, vulnerability, and reliability of coastal bridges susceptible to hurricane waves based on 3D numerical and experimental studies. The wave-structure interaction is simulated by a 3D CFD model, which is validated by experimental measurements. The external wave forces are then imported into the 3D FEM to further calculate the overturning moment, bearing reaction force, and working states. Surrogate models are examined to quantify wave force and overturning moment with different parameters for cases which the empirical method could not well predict. Based on the numerical results, a new component-level bridge overturning failure mode is developed, which considers the effects of the overturning moment and bearing damage. Limit states are defined, and criteria for each limit state are calculated from FEM. Given the fragility surface derived from the new overturning failure mode, long-term failure probability is assessed by considering climate change effects.

The conclusions are drawn as follows:

1. A 3D CFD model is established to simulate the wave-structure interaction and validated with experimental measurements. This model could better simulate the uneven force distribution on the deck and provide reliable results for its spatial advantage in x, y, and z directions. During the wave-structure interaction, the maximum vertical force on each deck component reduces, while horizontal force increases, from seaward to landward side.
2. A 3D FEM model is established to investigate the uneven wave force distribution on the deck and the resulting large overturning moment. The extreme overturning moment could destroy seaward bearings first, and the changed constraints would further affect the structural stability, causing the bridge deck to overturn.
3. For a more accurate prediction of structural response, different parameters are introduced to quantify the results under different surge and wave scenarios, including clearance Z_c and wave height H for unsubmerged conditions, wave steepness H/λ and initial trapped air ratio A_r for partially submerged conditions, and wavelength λ and submerged ratio M_r for fully submerged conditions.
4. Based on the 3D numerical results, a new component-level bridge overturning failure mode is developed by considering the effects of the overturning moment, bearing damage, and failure sequence. Each damage level is defined according to the degree of structural damage, and limit states are computed with FEM.
5. It is demonstrated that the overturning failure mode could identify component-level damage of the bridge and calculate a larger failure probability for the investigated

case as compared with the unseating mode. It is suggested by the authors that both failure modes should be considered in future studies since the structural responses vary and depend on wave forms as well as structural dimensions.

6. It is concluded that the bridge failure probability could increase by up to 40% during a 30-year period and by over 90% for a 100-year period when considering climate change effects. The increment in hurricane scale has a great impact on the bridge failure probability since it affects multiple demand parameters such as surge and wave heights.

The proposed framework can aid the robust design and management of coastal bridges subjected to hurricanes in a life-cycle context by considering different failure modes (e.g., uplift, overturning) and reliability. Future studies are expected to examine the structural responses and bearing performance of a bridge under oblique wave effects, to assess the monetary loss caused by the hurricanes, and to consider the deterioration effects of RC structures in the reliability assessment.

Acknowledgments

The study has been supported by National Key R&D Program of China (No. 2019YFB1600702), and Research Grant Council of Hong Kong (No. T22-502/18-R and ECS project No. PolyU 252161/18E). The opinions and conclusions presented in this paper are those of the authors and do not necessarily reflect the views of the sponsoring organizations.

Notation

The following symbols are used in this paper:

A_g = cross-sectional area of girders;

A_r = initial trapped air ratio;

C_d = design clearance;

C_F = structural capacity of unseating failure mode;

C_M = structural capacity of overturning failure mode;

c = wave celerity;

D = water depth;

D_F = structural demand of unseating failure mode;

D_M = structural demand of overturning failure mode;

d_b = deck thickness;

d_g = girder height;

F = fetch length;

F_x = horizontal wave force on bridge span;

F_y = vertical wave force on bridge span;

f_{Li} = reaction force of the i^{th} bearing on the span L side;

f_{Ri} = reaction force of the i^{th} bearing on the span R side;

f_{xi} = horizontal wave force on the i^{th} bridge section;

f_{yi} = vertical wave force on the i^{th} bridge section;

f_c' = ultimate concrete compressive strength;

f_t' = axial tensile cracking stress;

G = limit state function;

H = wave height;

H_{mode} = mode wave height;

H_s = significant wave height;

L_{Fhi} = horizontal moment arm;

L_{Fvi} = vertical moment arm;

L_m = bridge length in model scale;

L_p = bridge length in prototype scale;

l = span length;

M = overturning moment on bridge span;

M_r = submerged ratio;

m = model predictors;

n_g = girder number;

O = moment center;

q = number of total predictors;

r_α = increment rate in maximum wind speed;

r_ω = increment rate in hurricane occurrence rate;

S = surge height;

T = investigated time interval in year;

t = time;

t_0 = time interval between wave crest and still water level;

U_A = wind stress factor;

$U_{\max}$ = maximum wind speed;

W = deck width;

W_s = deck weight;

y = observed values;

$y_{\max}$ = maximum sample in the subsample;

y_{mean} = mean value of the samples;

$y_{\min}$ = minimum sample in the subsample;

y' = approximating function;

Z_c = clearance;

α = scale parameter;

β = shape parameter;

γ = unit weight of deck;

λ = wavelength;

ε_c = concrete strain;

ε_{cu} = ultimate concrete strain;

ε_0 = peak concrete strain;

η = water surface elevation;

θ = model parameters;

σ = scale parameter of Rayleigh distribution;

σ_c = concrete stress;

τ = scale ratio;

ω = mean annual hurricane occurrence rate.

References

[1] Lukic, E., (2009). Review of Hurricane Wilma Expenditures and Reimbursements.

[2] Hall, B. J. *et al.*, (2019). The association between disaster exposure and media use on post-traumatic stress disorder following Typhoon Hato in Macao, China. *European Journal of Psychotraumatology*, *10* (1), 1558709.

[3] Frangopol, D. M., Dong, Y., and Sabatino, S., (2017). Bridge life-cycle performance and cost: analysis, prediction, optimisation and decision-making. *Structure and Infrastructure Engineering*, *13* (10), 1239–1257.

[4] Li, Y., Dong, Y., and Qian, J., (2020). Higher-order analysis of probabilistic long-term loss under nonstationary hazards. *Reliability Engineering and System Safety*, *203*.

[5] Ataei, N. and Padgett, J. E., (2013). Probabilistic modeling of bridge deck unseating during hurricane events. *Journal of Bridge Engineering*, *18* (4), 275–286.

[6] Guo, A., Fang, Q., Bai, X., and Li, H., (2015). Hydrodynamic Experiment of the Wave Force Acting on the Superstructures of Coastal Bridges. *Journal of Bridge Engineering*, *20* (12), 1–11.

[7] Cuomo, G., Shimosako, K. ichiro, and Takahashi, S., (2009). Wave-in-deck loads on coastal bridges and the role of air. *Coastal Engineering*, *56* (8), 793–809.

[8] Cai, Y., Agrawal, A., Qu, K., and Tang, H. S., (2018). Numerical Investigation of Connection Forces of a Coastal Bridge Deck Impacted by Solitary Waves. *Journal of Bridge Engineering*, *23* (1), 04017108.

[9] Xu, G., Cai, C. S., Hu, P., and Dong, Z., (2016). Component Level–Based Assessment of the Solitary Wave Forces on a Typical Coastal Bridge Deck and the Countermeasure of Air Venting Holes. *Practice Periodical on Structural Design and Construction*, *21* (4),

04016012.

[10] Huang, W. and Xiao, H., (2009). Numerical modeling of dynamic wave force acting on Escambia bay bridge deck during Hurricane Ivan. *Journal of Waterway, Port, Coastal and Ocean Engineering*, *135* (4), 164–175.

[11] Xiao, H. and Huang, W., (2008). Numerical modeling of wave runup and forces on an idealized beachfront house. *Ocean Engineering, 35* (1), 106–116.

[12] Seiffert, B., Hayatdavoodi, M., and Ertekin, R. C., (2014). Experiments and computations of solitary-wave forces on a coastal-bridge deck. Part I: Flat Plate. *Coastal Engineering*, *88*, 194–209.

[13] Yuan, P., Xu, G., Chen, Q., and Cai, C. S., (2018). Framework of Practical Performance Evaluation and Concept of Interface Design for Bridge Deck-Wave Interaction. *Journal of Bridge Engineering*, *23* (7), 1–12.

[14] Jin, J. and Meng, B., (2011). Computation of wave loads on the superstructures of coastal highway bridges. *Ocean Engineering*, *38* (17–18), 2185–2200.

[15] Bozorgnia, M. and Lee, J. J., (2012). Computational fluid dynamic analysis of highway bridges exposed to hurricane waves. *Proceedings of the Coastal Engineering Conference*, 1–14.

[16] Zhu, D. and Dong, Y., (2020). Experimental and 3D numerical investigation of solitary wave forces on coastal bridges. *Ocean Engineering*, *209*, 107499.

[17] Padgett, J. *et al.*, (2008). Bridge damage and repair costs from Hurricane Katrina. *Journal of Bridge Engineering*, *13* (1), 6–14.

[18] Xu, G., Cai, C. S., and Han, Y., (2016). Investigating the characteristics of the solitary wave-induced forces on coastal twin bridge decks. *Journal of Performance of Constructed Facilities*, *30* (4), 4015076.

[19] Xu, G. and Cai, C. S., (2017). Numerical investigation of the lateral restraining stiffness effect on the bridge deck-wave interaction under Stokes waves. *Engineering Structures*, *130*, 112–123.

[20] Hayatdavoodi, M., Seiffert, B., and Ertekin, R. C., (2014). Experiments and computations

of solitary-wave forces on a coastal-bridge deck. Part II: Deck with girders. *Coastal Engineering*, *88*, 210–228.

[21] Huang, B., Zhu, B., Cui, S., Duan, L., and Zhang, J., (2018). Experimental and numerical modelling of wave forces on coastal bridge superstructures with box girders, Part I: Regular waves. *Ocean Engineering*, *149* (May 2017), 53–77.

[22] Li, Y., Dong, Y., Frangopol, D. M., and Gautam, D., (2020). Long-term resilience and loss assessment of highway bridges under multiple natural hazards. *Structure and Infrastructure Engineering*, *16* (4), 626–641.

[23] Chorzepa, M. G., Saeidpour, A., Christian, J. K., and Durham, S. A., (2016). Hurricane vulnerability of coastal bridges using multiple environmental parameters. *International Journal of Safety and Security Engineering*, *6* (1), 10–18.

[24] Ataei, N. and Padgett, J. E., (2015). Fragility surrogate models for coastal bridges in hurricane prone zones. *Engineering Structures*, *103*, 203–213.

[25] Saeidpour, A., Chorzepa, M. G., Christian, J., and Durham, S., (2019). Probabilistic hurricane risk analysis of coastal bridges incorporating extreme wave statistics. *Engineering Structures*, *182* (June 2018), 379–390.

[26] Huang, B., Yang, Z., Zhu, B., Zhang, J., Kang, A., and Pan, L., (2019). Vulnerability assessment of coastal bridge superstructure with box girder under solitary wave forces through experimental study. *Ocean Engineering*, *189*, 106337.

[27] Kameshwar, S. and Padgett, J. E., (2014). Multi-hazard risk assessment of highway bridges subjected to earthquake and hurricane hazards. *Engineering Structures*, *78*, 154–166.

[28] Arnold, C. D., (2012). Multi-Failure Mode Risk Assessment of the Houston/Galveston Bridge System to Hurricane Threats, 2012.

[29] Xu, G., Kareem, A., and Shen, L., (2020). Surrogate Modeling with Sequential Updating: Applications to Bridge Deck–Wave and Bridge Deck–Wind Interactions. *Journal of Computing in Civil Engineering*, *34* (4), 04020023.

[30] Li, Y., Dong, Y., and Zhu, D., (2020). Copula-Based Vulnerability Analysis of Civil

Infrastructure Subjected to Hurricanes. *Frontiers in Built Environment*, *6*, 170.

[31] Dong, Y. and Frangopol, D. M., (2017). Adaptation optimization of residential buildings under hurricane threat considering climate change in a lifecycle context. *Journal of Performance of Constructed Facilities*, *31* (6), 4017099.

[32] Tu, B., Fang, Z., Dong, Y., and Frangopol, D. M., (2017). Time-variant reliability analysis of widened deteriorating prestressed concrete bridges considering shrinkage and creep. *Engineering Structures*, *153*, 1–16.

[33] Elsner, J. B., Kossin, J. P., and Jagger, T. H., (2008). The increasing intensity of the strongest tropical cyclones. *Nature*, *455* (7209), 92–95.

[34] Bender, M. A. *et al.*, (2010). Modeled impact of anthropogenic warming on the frequency of intense Atlantic hurricanes. *Science*, *327* (5964), 454–458.

[35] Knutson, T. R. *et al.*, (2010). Tropical cyclones and climate change. *Nature geoscience*, *3* (3), 157–163.

[36] Douglass, S. L., Hughes, S. a, Rogers, S., and Chen, Q., (2004). The Impact of Hurricane Ivan on the Coastal Roads of Florida and Alabama: A Preliminary Report. *Rep. to Coastal Transportation Engineering Research and Education Center, Univ. of South Alabama, Mobile, Ala*, 1–19.

[37] ANSYS, (2016). Fluent Theory Guide 17.2. *Ansys Inc. USA.*

[38] Moideen, R., Behera, M. R., Kamath, A., and Bihs, H., (2018). Numerical Modelling of Solitary and Focused Wave Forces on Coastal-Bridge Deck. *Coastal Engineering Proceedings*, (36), 12.

[39] Boyd, J. P., (2007). Planetary solitary waves. *Solitary Waves in Fluids*, *47* (1994), 125.

[40] Constantin, A. and Escher, J., (2007). Particle trajectories in solitary water waves. *Bulletin of the American Mathematical Society*, *44* (3), 423–431.

[41] Munk, W. H., (1949). The Solitary Wave Theory and Its Application To Surf Problems. *Annals of the New York Academy of Sciences*, *51* (3), 376–424.

[42] Goring, D. G., (1978). Tsunamis - the Propagation of Long Waves Onto a Shelf. *Calif Inst Technol W M Keck Lab Hydraul Water Resour Rep KH-R*, (38).

[43] Robertsson, J. O. A. and Blanch, J. O., (2020). Numerical Methods, Finite Difference, 2020, 1–9.

[44] Chakrabarti, S. K., (2005). Physical Modelling of Offshore Structures, in *Handbook of Offshore Engineering*, 2005, 1001–1054.

[45] ACI Committee 318, (2014). Building Code Requirements for Structural Concrete, in *American Concrete Institute*, 2014, 524.

[46] Khaleghi, B. *et al.*, (2019). Experiences in the Performance of Bridge Bearings and Expansion Joints Used for Highway Bridges.

[47] Caltrans, (1994). Bridge memo to designers. Section 7: Bridge Bearings, California Department of Transportation Sacramento, CA.

[48] AASHTO, (2017). AASHTO LRFD bridge design specifications. *Washington: American Association of State Highway and Transportation Officials*.

[49] AASHTO, (2008). *Guide specifications for bridges vulnerable to coastal storms*. 2008.

[50] Box, G. E. P. and Wilson, K. B., (1951). On the experimental attainment of optimum conditions. *Journal of the royal statistical society: Series b (Methodological)*, *13* (1), 1–38.

[51] Simpson, T. W., Peplinski, J. D., Koch, P. N., and Allen, J. K., (2001). Metamodels for computer-based engineering design: Survey and recommendations. *Engineering with Computers*, *17* (2), 129–150.

[52] Longuet-Higgins, M. S., (1952). On the statisticaldistribution of the height of sea waves. *JMR*, *11*, 245–266.

[53] Casas-Prat, M. and Holthuijsen, L. H., (2010). Short-term statistics of waves observed in deep water. *Journal of Geophysical Research: Oceans*, *115* (C9).

[54] Feng, X., Tsimplis, M. N., Quartly, G. D., and Yelland, M. J., (2014). Wave height analysis from 10 years of observations in the Norwegian Sea. *Continental Shelf Research*, *72*, 47–56.

[55] Hashino, M., (1985). Characteristics of concurrence of rainfall, flood and storm surge associated with typhoon. *Journal of Hydroscience and Hydraulic Engineering*, *3* (2), 31–

47.

[56] Yue, S., (2000). The Gumbel logistic model for representing a multivariate storm event. *Advances in Water Resources*, *24* (2), 179–185.

[57] Wang, Y., Mao, X., and Jiang, W., (2018). Long-term hazard analysis of destructive storm surges using the ADCIRC-SWAN model: A case study of Bohai Sea, China. *International journal of applied earth observation and geoinformation*, *73*, 52–62.

[58] JCSS, (2001). *Probabilistic model code. Part 3: Resistance models*. 2001.

[59] CERC, (1984). Shore protection manual: Volume I and II. *Spm1984*.

[60] Liang, M. S. and Julius, S., (2011). On the Coastal Topography and Storm Surge for Infrastructure Risk Assessment and Adaptation, in *World Environmental and Water Resources Congress 2017*, 2011, 232–240.

[61] Zhu, D., Li, Y., Dong, Y., and Peng, Y., (2021) Long-term loss assessment of coastal bridges from hurricanes incorporating overturning failure mode. *Advance in Bridge Engineering*, DOI: 10.1186/s43251-020-00030-743251_2020_30.

[62] Batts, M. E., Cordes, M. R., Russell, L. R., Shaver, J. R., and Simin, E., (1980). Hurricane wind speeds in the United States. *Journal of the Structural Division*, *106* (10), 2001–2016.

[63] Peterka, J. A. and Shahid, S., (1998). Design gust wind speeds in the United States. *Journal of Structural Engineering*, *124* (2), 207–214.

[64] Li, Q., Wang, C., and Zhang, H., (2016). A probabilistic framework for hurricane damage assessment considering non-stationarity and correlation in hurricane actions. *Structural Safety*, *59*, 108–117.